Impacts of Ocean Currents on the South Indian Ocean Extratropical Storm Track through the Relative Wind Effect

HYODAE SEO,[a] HAJOON SONG,[b] LARRY W. O'NEILL,[c] MATTHEW R. MAZLOFF,[d] AND BRUCE D. CORNUELLE[d]

[a] *Woods Hole Oceanographic Institution, Woods Hole, Massachusetts*
[b] *Yonsei University, Seoul, South Korea*
[c] *Oregon State University, Corvallis, Oregon*
[d] *Scripps Institution of Oceanography, La Jolla, California*

(Manuscript received 16 February 2021, in final form 9 August 2021)

ABSTRACT: This study examines the role of the relative wind (RW) effect (wind relative to ocean current) in the regional ocean circulation and extratropical storm track in the south Indian Ocean. Comparison of two high-resolution regional coupled model simulations with and without the RW effect reveals that the most conspicuous ocean circulation response is the significant weakening of the overly energetic anticyclonic standing eddy off Port Elizabeth, South Africa, a biased feature ascribed to upstream retroflection of the Agulhas Current (AC). This opens a pathway through which the AC transports the warm and salty water mass from the subtropics, yielding marked increases in sea surface temperature (SST), upward turbulent heat flux (THF), and meridional SST gradient in the Agulhas retroflection region. These thermodynamic and dynamic changes are accompanied by the robust strengthening of the local low-tropospheric baroclinicity and the baroclinic wave activity in the atmosphere. Examination of the composite life cycle of synoptic-scale storms subjected to the high-THF events indicates a robust strengthening of the extratropical storms far downstream. Energetics calculations for the atmosphere suggest that the baroclinic energy conversion from the basic flow is the chief source of increased eddy available potential energy, which is subsequently converted to eddy kinetic energy, providing for the growth of transient baroclinic waves. Overall, the results suggest that the mechanical and thermal air–sea interactions are inherently and inextricably linked together to substantially influence the extratropical storm tracks in the south Indian Ocean.

KEYWORDS: Atmosphere-ocean interaction; Extratropical cyclones; Wind stress; Boundary currents; Storm tracks

1. Introduction

To date, two largely separate lines of research pertinent to extratropical air–sea interaction have convincingly demonstrated that midlatitude storm tracks are strongly influenced by their thermal interactions with sea surface temperature (SST) over western boundary current (WBC) regions, and that the energetics and stability of the WBCs themselves are controlled by their mechanical interaction with the atmosphere via surface currents. The former line of research posits that warm water masses carried by the Gulf Stream, Kuroshio, and Agulhas Current (AC) help sustain equatorward meridional temperature gradients in the lower troposphere against ceaseless erosion by poleward transient eddy heat fluxes (Nakamura et al. 2004, 2008), maintaining lower-tropospheric baroclinicity, a vital energy source for the growth of synoptic disturbances (Hoskins and Valdes 1990; Nakamura and Shimpo 2004). Over the warm portion of the WBCs, static stability in the lower troposphere is weakened under continuous influence of cold fronts or cold air outbreaks, which also enhances baroclinicity (Czaja and Blunt 2011; Small et al. 2019a; Czaja et al. 2019).

The close association among SST, baroclinicity, and storm track is illustrated in Fig. 1a for the south Indian Ocean, the focus of this study, with shading indicating the climatological maximum Eady growth rate at 850 hPa, a commonly used measure of the lower-tropospheric baroclinicity (Eady 1949; section 4a). One can find two maxima in the Eady growth rate: one that stretches zonally along the maximum SST gradients at 40°–50°S over the Antarctic Circumpolar Current (ACC) system, and another one, much stronger, that originates from the shores of South Africa associated with the warm AC. These regions of enhanced baroclinicity are aptly aligned with the regions of intense meridional SST gradient and warmer SST (contours in Figs. 1a,b), as well as the (negative) maxima in poleward eddy heat flux at 850 hPa (Fig. 1b). Given the robust connectivity between upstream and downstream storm tracks (Sinclair et al. 1997), with upstream perturbations feeding downstream adjustments via changes in the upper-level baroclinic wave structures (Chang 1993; Chang and Olanski 1993; Willison et al. 2013), the altered cyclogenesis over WBCs causes a host of modulations in the path and strength of the storm tracks downstream (Nakamura et al. 1997; Czaja et al. 2019).

As for the second line of research, in the ocean modeling community, in particular, the effect of considering the relative wind (RW; i.e., wind relative to ocean current) in surface wind stress calculation has long been considered critical for realistic

Corresponding author: Hyodae Seo, hseo@whoi.edu

DOI: 10.1175/JCLI-D-21-0142.1

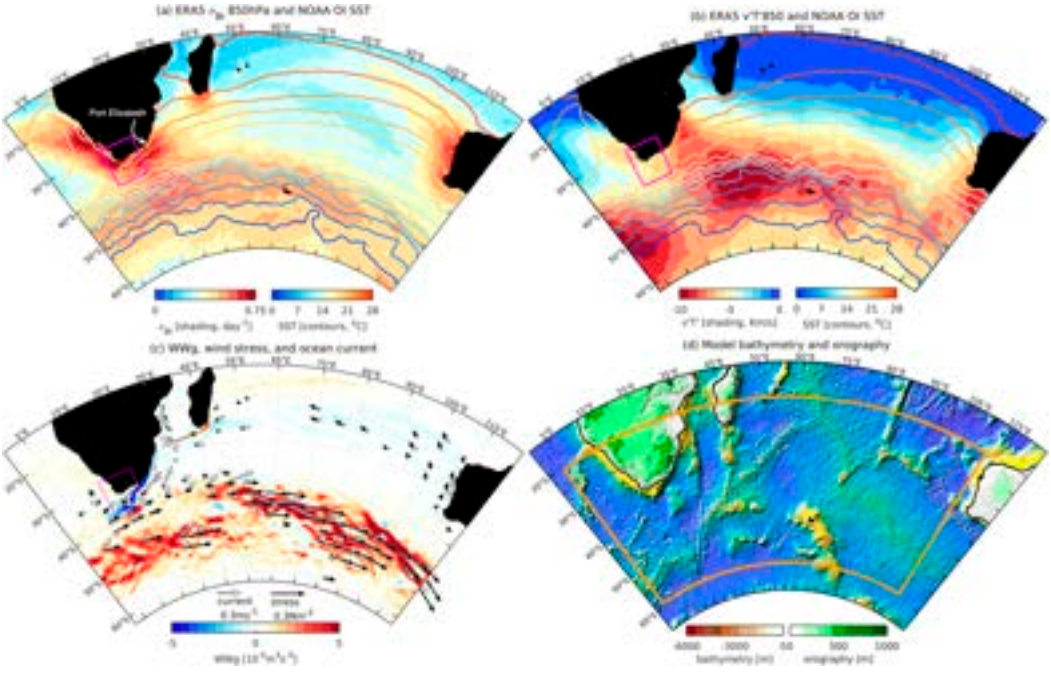

FIG. 1. Annual-mean (2011–15) maps of (a) maximum Eady growth rate ($|\boldsymbol{\sigma}_{\mathrm{BI}}|$) at 850 hPa ($\mathrm{day}^{-1}$), (b) poleward eddy heat flux ($\overline{v'T'}$) at 850 hPa ($\mathrm{K\,m\,s}^{-1}$), both estimated from ERA5 (shading), overlaid with the SST climatology (°C; contours) from NOAA optimum interpolation (OI) SST, and (c) total (mean + eddy) geostrophic wind work (WW_g; shading) based on AVISO geostrophic currents and wind stress computed from ERA-Interim wind (taking into account the AVISO geostrophic currents). The black (white) vectors overlaid are surface currents (wind stresses). Vectors are shown only when the geostrophic current speed is greater than $0.2\,\mathrm{m\,s}^{-1}$. (d) The bottom bathymetry and orography (shading) and the extent of the model domain (orange).

simulation of energetics and variability of ocean circulation (e.g., Pacanowski 1987; Eden and Dietze 2009; Braby et al. 2020). The RW effect is expressed via the bulk aerodynamic formula for wind stress (τ) as

$$\tau = \rho_a c_D(\mathbf{u}_a - \mathbf{u}_o)|\mathbf{u}_a - \mathbf{u}_o|, \tag{1}$$

with ρ_a the density of air, C_D the drag coefficient, and $\mathbf{u}_a$ ($\boldsymbol{u}_o$) the surface wind (current) velocity vectors. The damping of geostrophic surface currents by the RW effect, as discussed by Zhai et al. (2012), is illustrated in Fig. 1c, showing the climatological total (mean + eddy) geostrophic wind work (WW_g),

$$\mathrm{WW}_g = \frac{1}{\rho_o}\overline{\mathbf{u}_g \cdot \boldsymbol{\tau}}, \tag{2}$$

where $\mathbf{u}_g$ is the surface geostrophic current vector and the overbar denotes the time average). The WW_g is positive over much of the ACC and the Agulhas Return Current where $\mathbf{u}_g$ and $\boldsymbol{\tau}$ both point eastward. By decreasing the stress according to the bulk formula, the RW effect would result in a weaker positive WW_g (reduced wind energy), slowing down the mean currents (Luo et al. 2005; Renault et al. 2016; Seo 2017). In contrast, WW_g is negative over the AC, which flows westward against the prevailing westerly wind stress, in which case the RW effect would increase the stress and strengthen the negative WW_g (increased dissipation). Both scenarios yield significant damping of the ocean energy.

Renault et al. (2019) demonstrated that the KE damping is primarily due to altered eddy–mean flow interactions, whereby the RW effect weakens both inverse and forward energy cascades while diverting ocean energy to the atmosphere. Although a direct modulation of kinematic profiles of the wind in the marine atmospheric boundary layer (MABL) is not negligible (e.g., Song et al. 2006; Takatama and Schneider 2017), some of the previous studies document more significant indirect impacts on time-mean SSTs via changes in ocean circulation (Renault et al. 2017) and consistent changes in large-scale atmospheric circulation via air–sea interaction (Seo 2017).

This study dovetails the mechanical air–sea coupling via the RW effect into the thermal coupling between the extratropical storm track and the WBC SSTs by hypothesizing that local and downstream extratropical cyclone activity is influenced by their interaction with the SSTs, air–sea fluxes, and diabatic feedback processes modulated by the RW effect. Using high-resolution regional coupled model simulations resolving relevant spatial scales of air–sea momentum exchanges, combined with analyses of various ocean and atmospheric data-assimilative datasets, the study will focus on the AC, the WBC of the South Indian subtropical gyre, and its relation to the extratropical storm track.

The AC flows southwestward along the east coast of South Africa before separating from the continent and turning into the eastward Agulhas Return Current. The southern boundary of the Agulhas retroflection marks the northern edge of the subtropical front, featuring strong meridional SST gradients (Fig. 1a).

Moreover, there is a secondary retroflection of the AC off Port Elizabeth (25°E) associated with a standing anticyclonic eddy (Lutjeharms and van Ballegooyen 1984), which is maintained by meandering perturbations that are generated near the Natal Bight and grow as they propagate southward along the coast (Lutjeharms and Roberts 1988; Tsugawa and Hasumi 2010; Rouault and Penven 2011). In many ocean models, this standing eddy tends to be overly energetic (Biastoch et al. 2008), a biased feature ascribed to anomalous upstream retroflection of the AC (Lutjeharms and van Ballegooyen 1988).

The warm SSTs and SST gradients in the AC main retroflection are frequently observed to influence the MABL thermodynamics and kinematics. From aircraft measurements, Jury and Courtney (1991) observed dramatic increases in turbulent heat fluxes, equivalent potential temperatures, and MABL convective turbulence across the SST front (Rouault et al. 2000; Messager and Swart 2016). Satellite observations show that the thermal effects of the warm AC and meandering SST fronts extend beyond the air–sea fluxes and MABL winds, leaving discernible imprints in cloud liquid water, cloud-top temperatures, and temperature profiles (O'Neill et al. 2003, 2005; Liu et al. 2007; Perlin et al. 2014, 2020). Several studies demonstrate that warm SSTs of the AC serve as a significant source of heat and water vapor to coastal storms, adding to their rain-bearing capacity (Walker 1990; Jury et al. 1993; Mason 1995; Reason and Mulenga 1999; Singleton and Reason 2006; Nkwinkwa Njouodo et al. 2018). Comparing multi-ensemble atmospheric general circulation model simulations forced with realistic versus smoothed SST, Reason (2001) concluded that the inclusion of the AC's warm SST signature increases the cyclone track density over the Agulhas and winter rainfall over South Africa. The strengthened cyclone activity is carried over downstream, yielding enhanced storm track activity over the southeast Indian Ocean.

Renault et al. (2017) first quantified regional ocean circulation and local precipitation responses to the RW effect. One of the most notable findings is that the standing anticyclonic eddy off Port Elizabeth at 25°E is significantly weakened by the RW effect, conducive to an increased tendency for the westward occurrence in the Agulhas retroflection and leakage. As a result, the SST is increased by 1–2 K with the RW effect in the Agulhas retroflection, accompanied by a significant increase in local rainfall near the coastal regions of South Africa. However, they observed no significant atmospheric responses away from the Agulhas retroflection, partly because the domain did not extend farther eastward to encompass the entirety of the storm track in the south Indian Ocean. While the present study also concerns the oceanic adjustment to the RW effect, it places a greater emphasis on its nonlocal impacts on the energetics and dynamics of the extratropical storm track.

The paper is organized as follows. Section 2 describes the model, experiments, and datasets. Section 3 discusses the upper-ocean circulation response to the RW effect, including mechanical and diabatic damping processes and mixed layer heat balance. Section 4 examines the extratropical storm track responses, while section 5 considers available eddy potential energy balance for the extratropical synoptic disturbances. Section 6 is a summary and discussion.

2. Model, experiments, and datasets

a. Model and experiments

The study uses the Scripps Coupled Ocean–Atmosphere Regional (SCOAR) model (Seo et al. 2007, 2014), which couples the WRF-ARW (Skamarock et al. 2008) with the Regional Ocean Modeling System (ROMS; Shchepetkin and McWilliams 2005; Haidvogel et al. 2000), through the COARE bulk flux algorithm incorporated in ROMS (Fairall et al. 1996, 2003). Because the wind stress is computed outside the WRF, there is no explicit direct feedback by the altered wind stress on the atmosphere in the present analysis. Recent studies (Renault et al. 2016, 2017, 2019) suggest that wind response in the MABL to stress acts to partially offset the drag and re-energize the surface currents. Hence, the eddy damping effect is likely overestimated in the present study.

In WRF, the deep cumulus convection is represented through the new Tiedtke scheme (Zhang et al. 2017), the cloud microphysics by the WRF single-moment 6-class scheme (Hong and Lim 2006), and the planetary boundary layer (PBL) by the Yonsei University nonlocal scheme (Hong et al. 2006). The Goddard shortwave radiation scheme (Chou and Suarez 1999) and the Rapid Radiation Transfer Model-G (Iacono et al. 2008) are used for shortwave and longwave radiation. The land surface process is treated with the Noah land surface model (Chen and Dudhia 2001). In ROMS, the *K*-profile parameterization (KPP) scheme (Large et al. 1994) determines vertical eddy viscosity and diffusivity. The vertical grid in ROMS is stretched to enhance the resolutions near the surface and the bottom, using the so-called stretching parameters of $\theta_s = 7.0$, $\theta_b = 2.0$, and $h_{\text{cline}} = 300$ m.

The ocean and atmospheric models have identical horizontal grid spacing of 6.9 km in the meridional direction and 3.7–6.9 km in the zonal direction. Vertically, ROMS (WRF) is run with a stretched vertical grid with 30 (39) vertical levels. This gives the total number of grid points of $1637 \times 620 \times 30$ (39) for ROMS (WRF). The model domain (Fig. 1d) covers the south Indian sector of the Southern Ocean, with the southern African continent and the Agulhas retroflection in the northwestern part of the domain (Fig. 1a). The zonal distance of the domain ranges between 5200 and 9500 km, which captures a large part of if not the entire downstream extension of the storm track.

Prior to the coupled simulations, the 10-yr ROMS spinup simulation was conducted driven by the temperature and salinity climatologies from the Simple Ocean Data Assimilation (SODA; Carton and Giese 2008) and forced by the monthly surface flux climatology from the Comprehensive Ocean–Atmosphere Dataset (da Silva et al. 1994). The end state of the ocean spinup simulation is then used as the ROMS initial condition for the coupled run, driven by the same SODA data as the lateral boundary condition. The WRF is initialized on 0000 UTC 1 January 2010 and driven by ERA-Interim at the lateral boundaries (Dee et al. 2011).

The control simulation, dubbed RW, was conducted for 6 years (2010–15), where the RW effect is taken into account in the bulk formula of ROMS. A sensitivity experiment, which branches off from RW on 1 January 2011 and runs for 5 years until 2015, omits the RW effect (noRW). The rectified coupled responses to the RW effect is estimated as annual-mean differences between RW and noRW over the overlapping period of 2011–15. Although

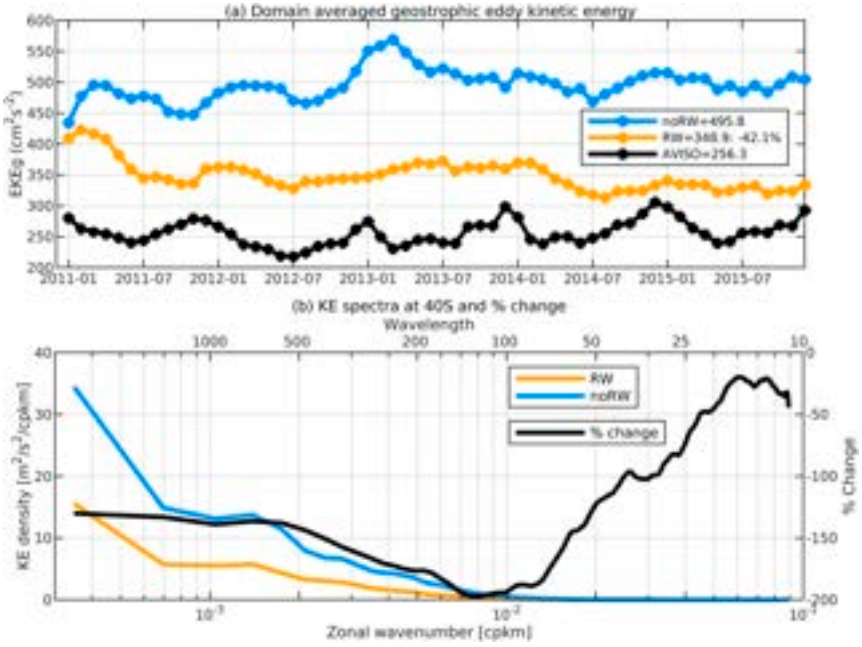

FIG. 2. (a) Time series of domain-averaged EKE_g ($cm^2\,s^{-2}$) and (b) total surface kinetic energy (KE) spectra ($m^2\,s^{-2}$ $cpkm^{-1}$) at 40°S in RW (orange) and noRW (blue). The black curve in (b) denotes the percentage change, defined as (RW − noRW)/RW × 100. Negative values correspond to a reduction of KE in RW. Zonal KE spectra were computed using the Welch's method, which breaks the input data into eight equal-length segments using a Hamming window with 50% overlap. The spectrum is calculated for each segment and then averaged to produce an estimate of the true spectra. The spectra in (b) cover 5-yr averages of the five-daily spectrum.

there are some interesting seasonal differences in the responses of the ocean and atmospheric fields (not shown), the current analysis focuses on annual mean differences. The RW effect is applied to both wind stress and turbulent heat flux. Although this study does not attempt to separate the two effects, our ongoing analysis indicates that the changes in the wind stress dominate the ocean temperature and circulation responses seen in this analysis (not shown). The statistical significance of the responses, marked as gray dots in figures, is assessed using a Monte Carlo simulation. The 5-yr RW and noRW runs are combined and randomly split into two sets of datasets. The difference between the two random samples is calculated each time, and the resampling process is repeated 1000 times to obtain the distribution of the random differences. The difference between the two simulations is then compared to the distribution of the random differences to calculate the two-sided significance levels at 95%, corresponding to the top and bottom 2.5th percentiles of the distribution.

Our choice of the model resolution (Δx = 3.7–6.9 km) is motivated by the need to resolve the relevant length scales to the RW effect and KE damping. For example, while the RW effect yields a significant reduction of surface KE by 42% when domain-averaged (Fig. 2a), the zonal wavenumber spectra at 40°S suggest that the KE damping is most markedly enhanced near the wavelength of ~100 km (Fig. 2b). The internal Rossby radius in the upper ocean, estimated as

$$\frac{Nh_{\mathrm{mix}}}{f},$$

where h_{mix} is the thickness of the near-surface boundary layer (Brink and Seo 2016), is 25–30 km at 40°S, consistent with the estimate of the first baroclinic Rossby radius of deformation by Chelton et al. (1998). This suggests that the RW effect constitutes a very effective damping mechanism of the KE at length scales commensurate with geostrophic eddy fields (Seo et al. 2019). This may have an important implication for the horizontal resolution requirements of coupled models to resolve the RW effect adequately. If one defines the effective resolution (Skamarock 2004; Soufflet et al. 2016) as 1/10 of this critical wavelength, the required model resolutions should be approximately 10 km at 40°S and decreasing poleward. A more accurate representation of the direct scale-to-scale air–sea momentum exchanges in a coupled model also requires the atmospheric model resolution to match the effective resolution of the ocean model (Jullien et al. 2020). The horizontal resolutions of the ocean and atmospheric models used in the present study meet these criteria.

b. Observational datasets

The following datasets are used for observational analysis and model evaluation. SST is from the daily 1/4° NOAA Optimum Interpolation SST dataset (Reynolds et al. 2007). The surface geostrophic current and sea surface height (SSH) datasets are obtained from Archiving, Validation, and Interpretation of Satellite Oceanographic Data (AVISO) produced by Ssalto/Duacs with support from CNES (http://www.aviso.altimetry.fr), available at 1/3° resolution. The wind stress used in Fig. 1 (and later in

Fig. 5) is estimated offline based on the COARE v3.5 bulk flux algorithm (Edson et al. 2013) using the ERA-Interim surface wind (Dee et al. 2011) and the AVISO geostrophic surface current. Because of the smooth nature of AVISO, however, the estimated wind work is likely to be biased (Chelton and Schlax 2003; Renault et al. 2016). The mixed layer heat budget (section 3) is computed using the 1/6° data-assimilating Biogeochemical Southern Ocean State Estimate (B-SOSE; Verdy and Mazloff 2017). The ERA5 (Hersbach et al. 2020) is used to estimate the turbulent and net heat fluxes (section 3) and to examine the storm track response (section 4) and the eddy available potential energy budget (section 5). All these observational products are on coarser grids than the model resolutions, which may have contributed to some discrepancies.

3. Dynamic and thermodynamic responses of the ocean

a. Time-mean response of the upper ocean

This section focuses on the dynamic and thermodynamic responses of the upper ocean relevant to air–sea interaction. Figure 3 compares, between the observations and model and between the two model simulations, the annual-mean geostrophic eddy kinetic energy (EKE_g; Figs. 3a–d), SSH overlaid with surface geostrophic current vectors (Figs. 3e–h), SST(Figs. 3i–l), and total turbulent heat flux (THF, positive downward; Figs. 3m–p) over the Agulhas retroflection. Figure 4 shows the same plots but over the whole model domain. In general, the model agrees reasonably well with the observed climatologies. However, one can identify several notable mean state biases. The simulated AC paths, as seen in the EKE_g, SSH, SST, and THF, are all spatially more variable west of Port Elizabeth toward the main Agulhas retroflection compared to the observational products. Given the strong coupling between SST and storm track in the WBCs and their extensions, the upper-ocean biases such as these may influence the simulation of storm track and its sensitivity to the oceans (Lee et al. 2018). Further discussions of the implications of the model biases are provided in section 6.

Between the two model simulations, the RW effect results in a significant reduction of EKE_g (42%; Fig. 2a). Over the Agulhas retroflection, the strongest EKE_g damping is observed in two regions: the anticyclonic standing eddy at 25°E and the main retroflection region farther south (15°–20°E). The weakened EKE_g in RW can be ascribed, at least partially, to a sink of eddy energy from the mesoscale ocean currents to the atmosphere (Fig. 5). Area-averaged mean geostrophic wind work (WW_{gm}) in RW is reduced by 77%, which in turn weakens EKE_g by 42% via baroclinic and barotropic energy conversions (Renault et al. 2017). There is also a significant contribution from the changes in eddy geostrophic wind work (WW_{ge}; Fig. 5h). It switches its sign from small positive ($+0.10 \times 10^5\,m^3\,s^{-3}$) in noRW to large negative in RW ($-0.33 \times 10^5\,m^3\,s^{-3}$), representing a substantial increase in direct damping of EKE_g (Seo et al. 2016; Renault et al. 2017; Song et al. 2020). The simulated WW_{gm} and WW_{ge} in RW are more consistent with the estimates based on observational datasets. Because of the weakened anticyclonic standing eddy at 25°E in RW, the AC continues its advection of warm water mass southwestward before retroflecting back into the south Indian Ocean. The increased westward retroflection of the AC with the RW effect was attributed to a reduction of the inverse energy cascade resulting from the weakened standing eddy (Renault et al. 2019). Since the prevailing wind stress is westerly south of 35°S (vectors), the ostensibly stronger negative WW_{gm} that stretches along the AC path in RW just indicates that the RW features stronger AC surface flow, which is subject to enhanced mechanical damping via altered wind stress. The resulting WW_{gm} and WW_{ge} in RW is more consistent with the observations, as evident from comparing Figs. 5a and 5b.

Recent studies show that, in regions of strong ocean currents and energetic eddy activity, SST variability is controlled by ocean advection, such that warm SST (or buoyancy) anomalies induce upward net heat (or buoyancy) flux anomalies (Bishop et al. 2017; Roberts et al. 2017; Small et al. 2020). This negative SST–heat flux covariance over the WBCs signifies the diabatic dissipation of ocean eddy available potential energy (EAPE), which in turn leads to weaker EKE via reduced baroclinic conversion (Ma et al. 2016; Yang et al. 2019; Bishop et al. 2020). One relevant question here is whether or not the reduced EKE with the RW effect corroborates the SST-induced diabatic damping mechanism. To answer this question, the thermal component of the EAPE generation term is computed, following Bishop et al. (2020), as the surface area (A) integral of correlation between perturbation surface temperature θ'_* and net heat flux Q'_s:

$$G_e = \int_A \frac{\alpha^2 g^2}{c_{po} N_r^2} \overline{\theta'_* Q'_s}\, dA, \tag{3}$$

where α is the thermal expansion coefficient, c_{po} the specific heat of seawater, g the gravitational acceleration, and N_r^2 the reference buoyancy frequency. The perturbation surface temperature is defined as $\theta_* = \theta - \theta_r(z)$, where $\theta_r(z)$ is a reference temperature. The primes denote the transient eddy components, calculated by removing the mean and seasonal cycle from the full daily fields. The G_e term is estimated from the B-SOSE and the two model simulations, with $\theta_r(z)$ and N_r^2 values from the B-SOSE used for the model simulations. Comparison of the absolute value of the G_e term is not meaningful in that a full budget calculation is not considered in this study. Taking the reference values from the observational dataset, however, facilitates the comparisons with the model simulations (Bishop et al. 2020).

Figures 5i–k compare the annual-mean G_e. The B-SOSE and the two runs all show the negative G_e, indicating the diabatic damping of EAPE. The difference shows that the RW simulation experiences weaker diabatic dissipation than the noRW run by 10%. That is, while the weaker EKE in RW is consistent with the enhanced mechanical damping (less positive WW_{gm} and more negative WW_{ge}; Figs. 5d,h), it does not corroborate the weaker diabatic damping (less negative G_e; Fig. 5l). Therefore, the weakened diabatic damping of eddy potential energy by the surface fluxes is unlikely to account for the reduced geostrophic eddy energy with the RW effect.

The anomalous southwestward extension of the warm AC in RW results in a significant increase in SST over the Agulhas retroflection of up to 2.7 K (1.1 K if area-averaged; Fig. 3l). There are also localized regions of significant warming (e.g., 40°S, 45°E) and of moderate cooling downstream due in part to subtle shifts of the subtropical front (Fig. 4i). However, the most robust changes in

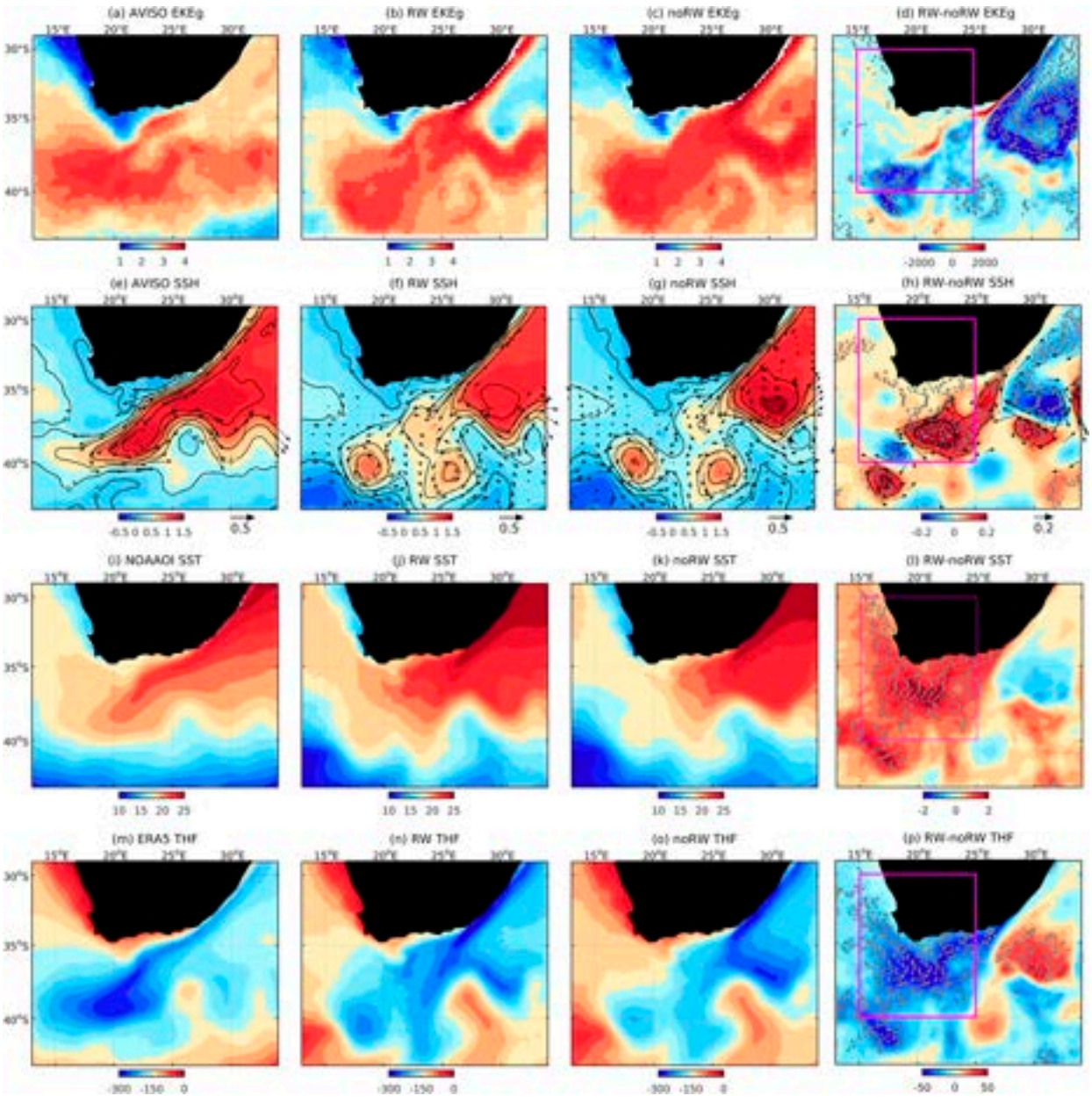

FIG. 3. Annual-mean maps of (a)–(d) surface geostrophic eddy kinetic energy [EKE_g; $cm^2\,s^{-2}$; (a)–(c) are in log-scale], (e)–(h) SSH (m) overlaid with the geostrophic surface current ($m\,s^{-1}$), (i)–(l) SST (°C), and (m)–(p) net turbulent heat flux (latent + sensible, $W\,m^{-2}$, positive downward). Columns show (left to right) the observed estimates, RW, noRW, and the difference between RW and noRW. The magenta box represents the Agulhas retroflection (30°–40°S, 15°–25°E).

SST are found in the Agulhas retroflection region. There, the SST warming in RW is accompanied by enhanced SSH (Fig. 3h) and increased upward THF exceeding $80\,W\,m^{-2}$ ($30\,W\,m^{-2}$ if area-averaged, 15% of the mean; Fig. 3p). This 1.1-K SST warming in the Agulhas retroflection due to the RW effect far exceeds the interannual SST standard deviation estimated from the model simulations over the same area (0.6 K in RW and 0.9 K in noRW).

The latitude–depth cross sections (Fig. 6) further illustrate the consequences of the circulation responses to the upper-ocean thermohaline and density structure. The water mass of subtropical origin with higher temperature and salinity and lower density advected by the AC occupies the top 1000 m in 35°–40°S in RW (shading). The outcropping latitudes of the isotherms, isohalines, and isopycnals (contours) are consistently shifted southward by ~1° near the subtropical front, leading to the strengthening of the meridional SST front.

b. *Upper-ocean heat budget*

The physical processes leading to the SST increase near the Agulhas retroflection can be further quantified by the mixed

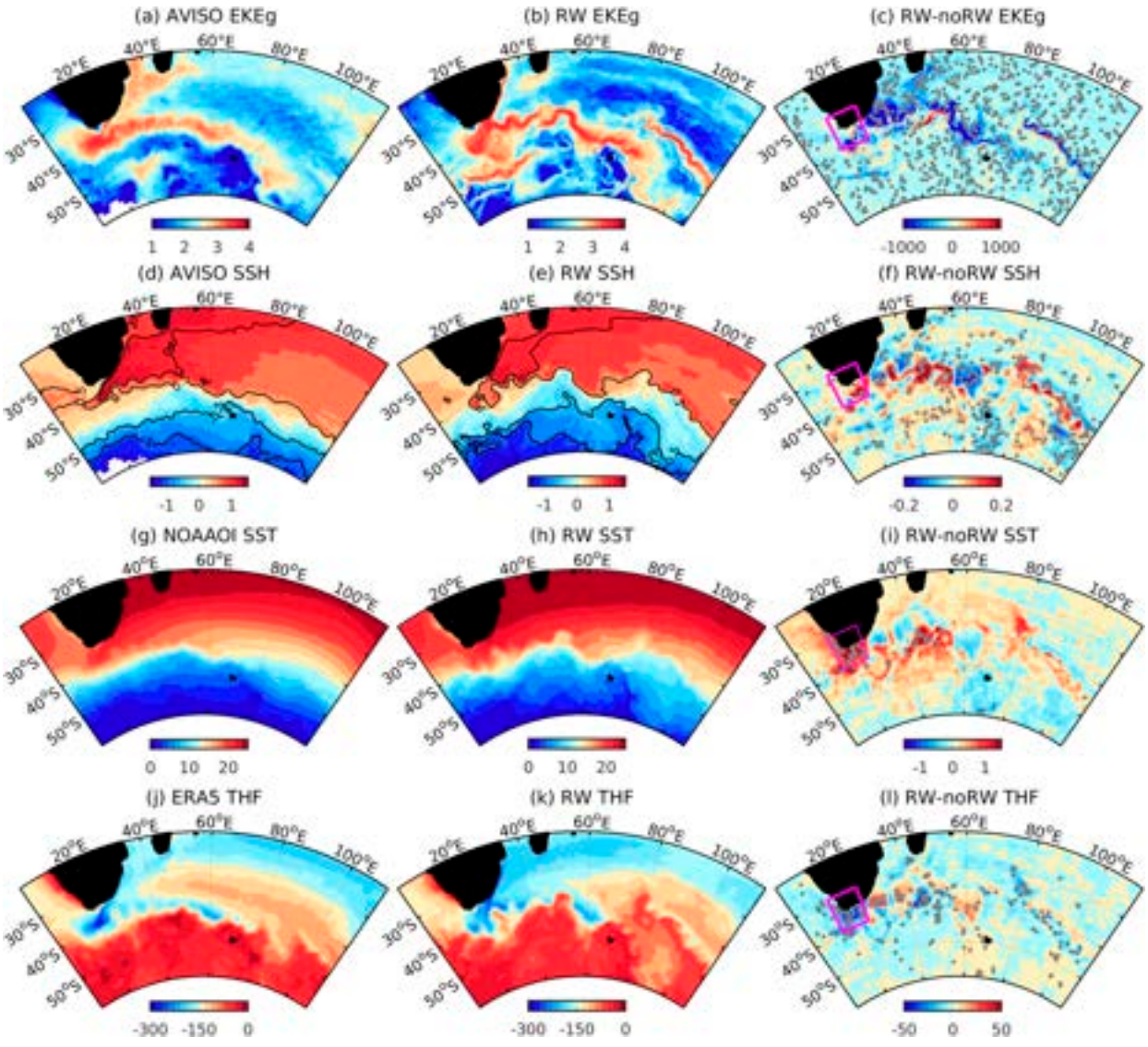

FIG. 4. As in Fig. 3, but for the entire model domain.

layer (ML) heat budget analysis. The vertically averaged ML heat budget equation derived from the conservation of mass and heat equations (Moisan and Niiler 1998) can be simplified as

$$\frac{\partial\langle T\rangle}{\partial t} = -\langle\mathbf{u}\rangle\cdot\nabla_H\langle T\rangle - \frac{1}{h}\nabla_H\cdot\int_{-h}^{0} u'T'\,dz + \frac{Q_s}{\rho_o c_{po} h} + R, \quad (4)$$

where $\langle T\rangle$ and $\langle\mathbf{u}\rangle$ are the temperatures and horizontal velocity vectors averaged over the ML depth, $h(x, y, t)$, which was computed using the density criteria of 0.03 kg m^{-3}. Also, ∇_H is the horizontal gradient operator, ρ_o the density of seawater, and Q_s is the net surface heat flux corrected for the penetrative solar radiation. The first and second terms on the right-hand-side (RHS) of Eq. (4) denote the horizontal mean and eddy heat advection respectively, which can be subsequently expressed as

$$-\frac{1}{h}\int_{-h}^{0}\left(\overline{\mathbf{u}}\cdot\nabla_H\overline{T} + \mathbf{u}'\cdot\nabla_H\overline{T} + \overline{\mathbf{u}}\cdot\nabla_H T' + \overline{\mathbf{u}'\cdot\nabla_H T'}\right)dz,$$

where the overbars represent the time mean. The last term R represents the residual, including vertical advection, entrainment, and the turbulent heat fluxes at the bottom of MLD, and the contributions from errors associated with discretization and interpolation. Each of the terms except for R is calculated using the five-daily outputs from RW and noRW and is compared to the respective terms calculated based on the B-SOSE.

Figure 7 shows the annual-mean ML temperature tendency, the total divergence of temperature transport, and the surface heat flux. Figure 8 breaks down the terms in the model simulations via area averaging. Variation of the domain size for averaging within the Agulhas retroflection does not significantly alter the results (not shown). As expected, the dominant ML heat balance is between

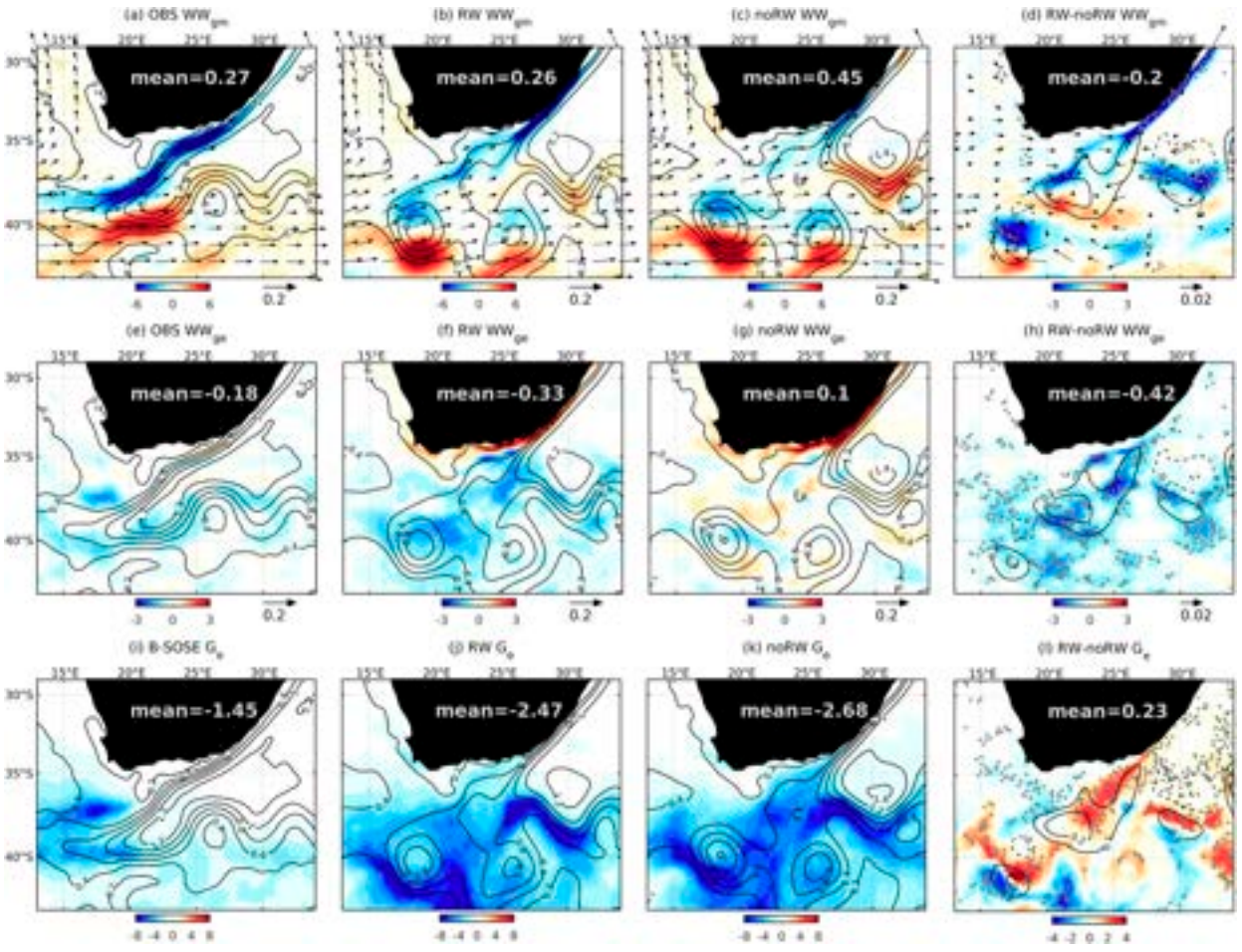

FIG. 5. Annual-mean maps of (top) geostrophic mean wind work (WW_{gm}; $10^{-5}\,m^3\,s^{-3}$), (middle) geostrophic eddy wind work (WW_{ge}; $10^{-5}\,m^3\,s^{-3}$), and (bottom) the generation of eddy available potential energy (G_e; $mW\,m^{-2}$) estimated from (a),(e),(i) observational products, (b),(f),(j) RW, (c),(g),(k) noRW, and (d),(h),(l) RW-noRW. The observational estimates for (a) WW_{gm} and (e) WW_{ge} are based on AVISO geostrophic current and ERA-I wind stress (taking into account the AVISO current), and (e) G_e from B-SOSE. The contours and vectors overlaid represent the SSH (m; CI = 0.2 m) and wind stress ($N\,m^{-2}$). The mean values shown in each plot are based on area-averaging over the magenta box.

the total convergence of ocean temperature advection and the surface heat flux (Tamsitt et al. 2016), with the former maintaining the upper-ocean warming despite the continuous damping by the latter. Consistent with the interpretation of the increased southwestward extension of the AC, the increased meridional temperature advection almost entirely accounts for the warming tendency. The change in mean horizontal advection is relatively small ($-19\,W\,m^{-2}$) compared to that in eddy advection is significant ($+152\,W\,m^{-2}$), suggesting that increased convergence is mainly attributed to the changes in eddy fields. Also, the interannual standard deviations of each of the terms, denoted as the error bars in Fig. 8, are consistently smaller in RW than noRW, another indication of the stabilized flow fields under the RW effect (Seo et al. 2016).

In summary, the local warming results in two types of upper-ocean responses relevant to air–sea interaction and storm track. First, the warmer SST under persistent westerlies enhances the annual-mean THF by up to $80\,W\,m^{-2}$. Is this increased turbulent heat loss to the atmosphere significant enough to destabilize the lower troposphere and possibly affect the tropospheric baroclinicity? Second, the southwestward extension of the warm AC in RW strengthens the SST front along the subtropical front; will the resulting increase in the meridional SST gradient alter the lower-tropospheric temperature gradient and thus its baroclinicity? We will further probe these two questions in the next section.

4. Extratropical storm track responses

This section examines how the dynamic and thermodynamic adjustments in the upper ocean discussed in the previous section are accompanied by the local and downstream changes in the extratropical cyclone activity.

a. Eulerian storm track diagnostics

To examine the changes in the storm track, we first consider four commonly used Eulerian storm track diagnostics. The

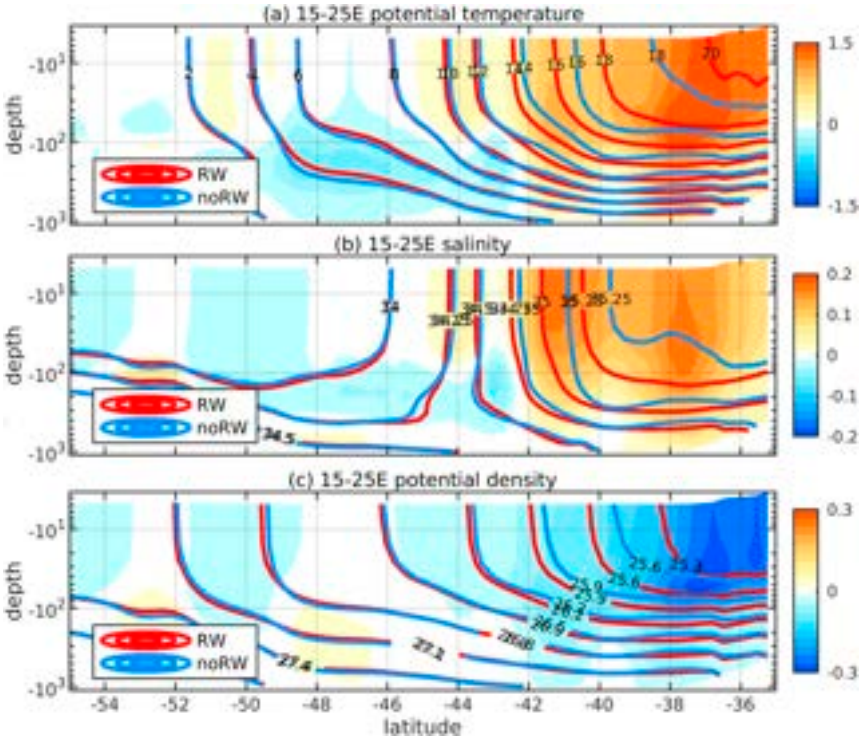

FIG. 6. Depth–latitude diagrams of annual-mean differences in (a) potential temperature (°C), (b) salinity (psu), and (c) potential density (kg m^{-3}), averaged over 15°–25°E. The red and blue contours denote the isotherms, isohalines, and isopycnals in RW and noRW, respectively.

four chosen Eulerian diagnostics emphasize different aspects of storm track (baroclinicity, eddy heat transport, MABL stratification, and extreme storms), allowing for a robust investigation of the storm track responses to SST changes. The first is the Eady growth rate, defined as the most unstable baroclinic mode, whose growth rate is scaled as the magnitude of the baroclinicity vector (Charney 1947; Eady 1949; Lindzen and Farrell 1980):

$$|\boldsymbol{\sigma}_{\mathrm{BI}}| = 0.31\left(\frac{g}{N\theta}\right)\left|-\frac{\partial\theta}{\partial y}, \frac{\partial\theta}{\partial x}\right| \tag{5}$$

Here, N is the buoyancy frequency and θ is the potential temperature.

Figures 9a and 9b show the annual-mean $|\boldsymbol{\sigma}_{\mathrm{BI}}|$ at 850 hPa from ERA5 and RW. There are two zones of enhanced $|\boldsymbol{\sigma}_{\mathrm{BI}}|$. The first is in the main storm track along 40°–50°S (Sinclair et al. 1997; Hoskins and Hodges 2005) over the warmer flank of the ACC (Dong et al. 2006), which, through its meridional SST gradients, maintains a steady and persistent near-surface baroclinic environment (Sinclair 1995; Nakamura et al. 2004; Hotta and Nakamura 2011). An additional maximum of $|\boldsymbol{\sigma}_{\mathrm{BI}}|$ exists directly over the Agulhas retroflection, which extends southeastward and merges with the main storm track east of 40°E. Between RW and noRW, a statistically significant increase in $|\boldsymbol{\sigma}_{\mathrm{BI}}|$ is found over the Agulhas retroflection. There is also increased $|\boldsymbol{\sigma}_{\mathrm{BI}}|$ along the southeast path toward the main storm track, although the differences downstream are not significant.

One can separate the contribution to changes in $|\boldsymbol{\sigma}_{\mathrm{BI}}|$ by the tropospheric temperature gradient from static stability (Fig. 10). The decomposition reveals that, over much of the domain, the contribution by the change in temperature gradient dominates, while the reduced static stability is concentrated in the Agulhas retroflection of the most robust SST increase. It is estimated that the contributions of the two terms to the total change are nearly the same in the Agulhas retroflection. Figure 10 also suggests that the difference in $|\boldsymbol{\sigma}_{\mathrm{BI}}|$ due to the temperature gradient and static stability is pronounced primarily over the secondary maximum of $|\boldsymbol{\sigma}_{\mathrm{BI}}|$ and is reasonably well separated from the main storm track farther south. This allows us to interpret the downstream storm track responses in terms of SST change in the Agulhas retroflection.

The annual-mean poleward transient eddy heat flux $\overline{v'T'}$ at 850 hPa, constitutes another variance-based measure of the storm track, where the primes denote 2–8-day filtering and the overbar the time mean. The negative $\overline{v'T'}$, signifying the poleward eddy heat flux (Figs. 9d–e), originates from the southeast of Africa and tracks southeastward with the maxima at 40°–50°S, 40°–60°E. The simulated annual-mean (Fig. 9e) and seasonal climatologies (not shown) are reasonable compared to the reanalysis (Fig. 9d) and the published results (e.g., Nakamura et al. 2004). The difference shows the increased (decreased) poleward eddy heat flux in RW south (north) of the maximum $\overline{v'T'}$, although the increase is not as apparent as the decrease. The maximum difference is found farther downstream at 40°–50°S, 70°E. However, the responses are not significant.

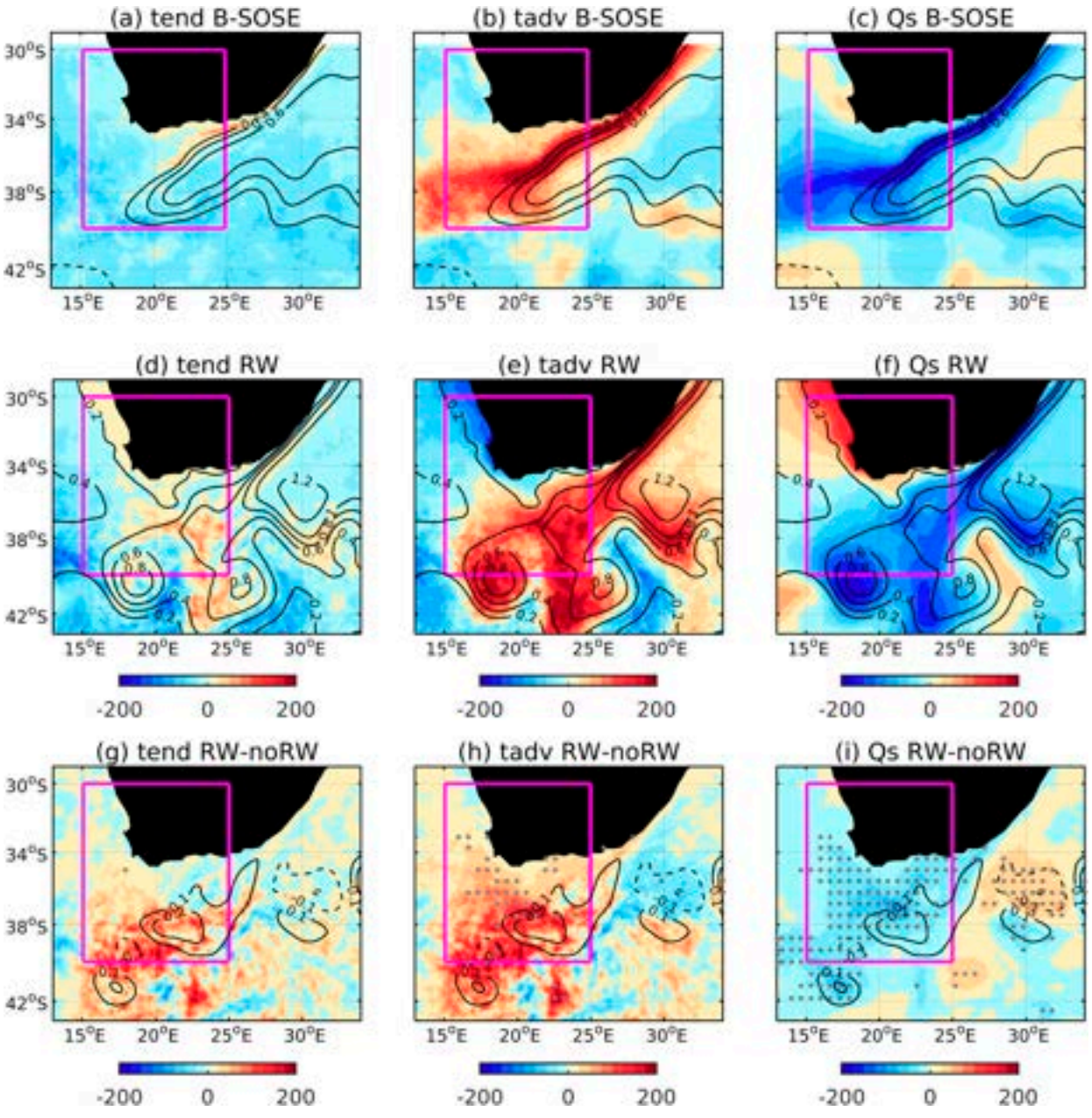

FIG. 7. Maps of annual-mean mixed layer heat budget terms (W m^{-2}) from (top) B-SOSE, (middle) RW, and (bottom) RW-noRW). See Eq. (4). The black contours denote the SSH (CI = 0.2 m for B-SOSE and RW and 0.1 m for RW − noRW).

An additional measure of the storm track based on surface wind, the so-called surface storm track (Booth et al. 2010, 2017b; O'Neill et al. 2017; Small et al. 2019b), is defined as the climatology of the yearly or seasonal standard deviation of $\tilde{v}$, where

$$\tilde{v}(t) = \frac{v_{10}(t+1) - v_{10}(t)}{2}. \tag{6}$$

Here, v_{10} is the daily meridional wind at 10 m. The conceptual framework of surface storm track is derived from earlier scatterometry-based studies (Sampe and Xie 2007; O'Neill et al. 2017), which identified a strong manifestation of the free-tropospheric storm tracks in the surface wind over the warm WBCs. This leads to an increased probability of high-wind occurrences via reduced static stability and induced vertical mixing (Wallace et al. 1989). As in $\overline{v'T'}$, the surface storm track (Figs. 9g–i) originates from the southeast coast of Africa and extends southeastward, but it tends to stay slightly equatorward of $\overline{v'T'}$ (Booth et al. 2017b). RW reasonably well represents the observed climatological pattern, albeit with weaker amplitude. The difference shows the significant increase in the surface storm track over the Agulhas

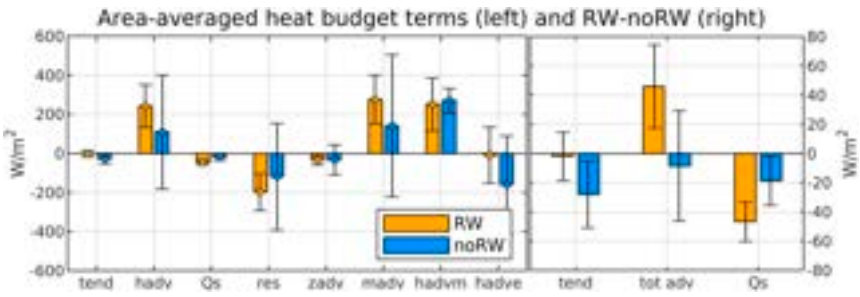

FIG. 8. Area-averaged (over the magenta box) mixed layer heat budget terms; tend is for tendency, hadv the total horizontal advection (mean + eddy), Q_s the surface flux, res the residual term, zadv the zonal advection, madv the meridional advection, hadvm the mean advection, hadve the eddy advection, and tot adv for total (horizontal advection + residual term, which includes vertical advection). The error bars denote ±1 interannual standard deviation of each term.

retroflection. It also shows the southeastward extension of the increased surface storm track in RW, but the downstream responses are not significant.

Finally, the low deepening rate (LDR) is a measure of explosive cyclone activity, defined by Kuwano-Yoshida and Minobe (2017) as

$$\mathrm{LDR} = \frac{p_s(t+24\mathrm{h}) - p_s(t-12\mathrm{h})}{24}\left|\frac{\sin 60^\circ}{\sin\alpha}\right|, \qquad (7)$$

where p_s is the 12-hourly sea level pressure (SLP) and α the latitude. The monthly cyclone activity is estimated by positive values of LDR. The LDR is largely zonally uniform in the ERA5 and RW (Figs. 9j–k). The difference illustrates the increased activity of intense cyclones both near the Agulhas retroflection and downstream (Fig. 9l).

b. *Composite evolution of the storms attuned to high-THF events*

The Eulerian storm track diagnostics considered in the previous subsection are based on all storm conditions. One could instead consider composite storm evolution that is directly related to the high-THF events in the Agulhas retroflection (Ma et al. 2015a,b). First, we define the high-THF events as when the 2–8-day band-passed THF averaged over Agulhas retroflection exceeds the negative one standard deviation. The 2–8-day filtered SLP and 500-hPa geopotential height (Z500) are then composited according to the identified high-THF events. Multiple peaks occurring within an 8-day window are counted as one event. This way, a total of 82 (87) events are identified in RW (noRW) for the 5-yr analysis period, translating to an average of 16.4 (17.4) storm counts per year. Then, the lagged composite anomalies of 2–8-day band-passed SLP and Z500 are constructed from day −5 to day +5, with day +0 corresponding to the time of the maximum THF.

The first (third) column of Fig. 11 shows the lagged composite evolution of SLP (Z500) anomalies normalized by their respective minima at the storm center on day −3. The composite evolution shows the quintessential characteristics of eastward propagating midlatitude baroclinic wave patterns, both at the surface and the midtroposphere, with the apparent westward tilt in troughs with height (Chang 1993). The space–time structure of the simulated composite storms is similar to that based on ERA5 (not shown). On day −2, a cyclonic anomaly is located southwest of the high THF with a weak anticyclone to its southeast. The system moves eastward at a speed of roughly 10° longitude day^{-1}, and on day +0 the cyclone is located south or southeast of the Agulhas retroflection. The southerly wind anomaly over the increased SST by the Agulhas retroflection energizes the turbulent heat loss from the ocean, while the emerging anticyclone to its west augments the intensity of the southerly wind. The storm gradually subsides as it moves eastward, as evident by the eastward decay in both SLP and Z500 anomalies. The second (fourth) column of Fig. 11 shows the composite difference in SLP (Z500) anomalies. The significant deepening (blue shading) of the cyclone in RW (orange contours) is found from day+0 onward, with the conspicuous intensification lasting until day +4, at which point the SLP and Z500 anomalies at the storm center are reduced by at least 10%–25%.

Hence, the analyses of multiple storm track metrics and composite evolution of storms directly associated with the SST/THF changes in the Agulhas retroflection illustrate the consequence of sea surface warming and strengthening of the meridional SST gradient by the RW effect. Over the Agulhas retroflection, where the oceanic forcing of the low-level baroclinicity is strongest, the storm track achieves significant intensification. Farther downstream, this analysis hints at the strengthening of the secondary storm track extending from Africa to merge with the main storm track. However, due to the large internal variability of the Southern Hemisphere atmosphere and the short simulations (5 years), the analysis based on the Eulerian diagnostics generally cannot confirm the robustness of the downstream responses. When considering only the storms directly attuned to the high SST/THF in the Agulhas retroflection, however, one finds more convincing evidence of the consistent strengthening of storm intensity, both at the surface and midtroposphere, both locally and downstream.

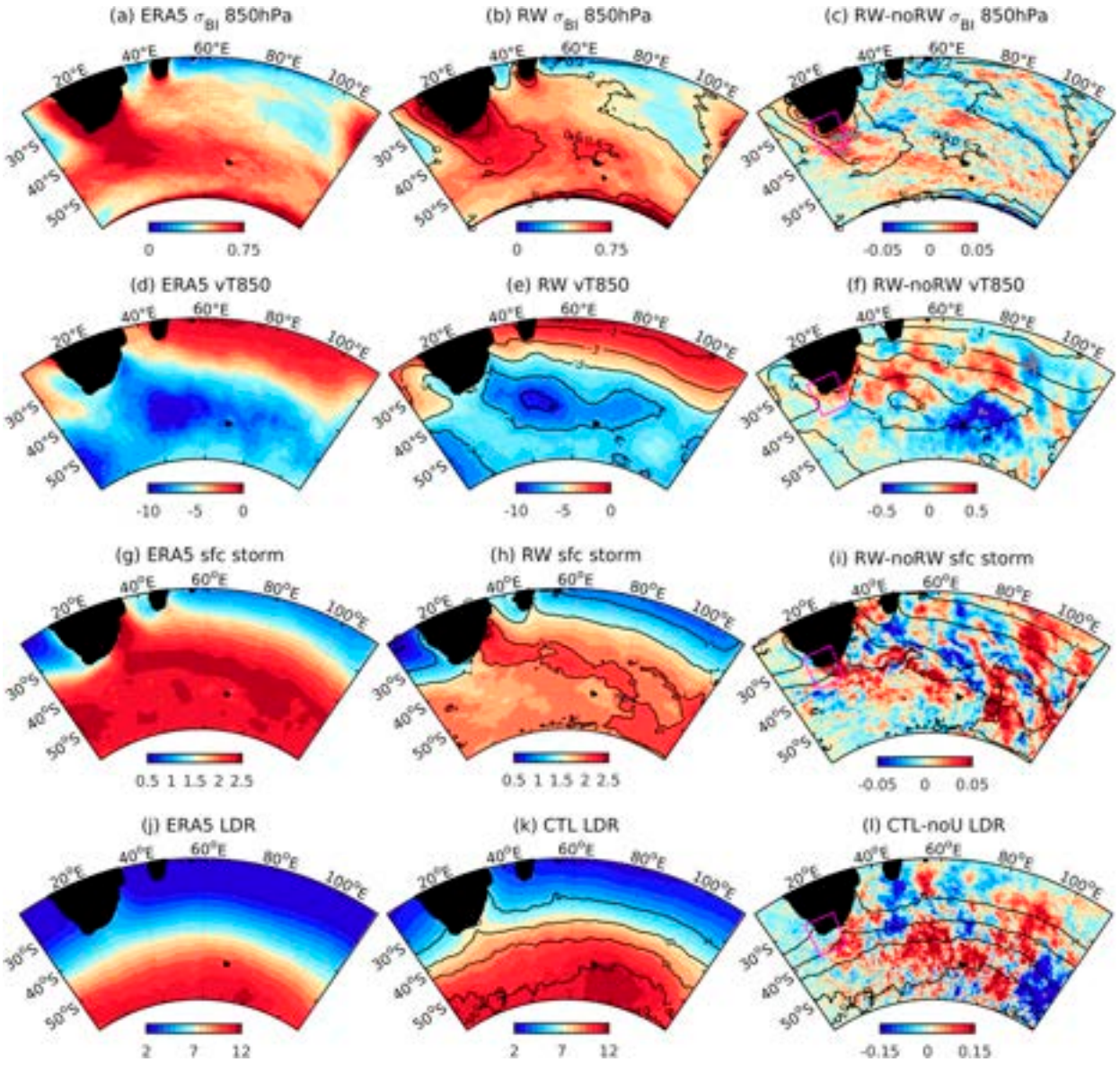

FIG. 9. (a) Annual-mean (a)–(c) $\boldsymbol{\sigma}_{\mathrm{BI}}$ at 850 hPa (day^{-1}), (d)–(f) $\overline{v'T'}$ at 850 hPa (m s^{-1} K), (g)–(i) surface storm track (m s^{-1}), and (j)–(l) low deepening rate (LDR; hPa day^{-1}) from (left) ERA5, (middle) RW, and (right) RW − noRW.

5. Eddy available potential energy balance

This section examines the storm track response from the perspective of an energy conversion framework by examining the eddy available potential energy (EAPE) budget for extratropical synoptic baroclinic disturbances. Following Lau and Lau (1992), the EAPE budget is cast as

$$\frac{\partial A_T}{\partial t} \approx \underbrace{\frac{c_{pa}\gamma}{\overline{T}}\overline{\mathbf{V}'_H T'}\cdot\nabla_H\overline{T}}_{\mathrm{PI}} + \underbrace{\frac{R\overline{T'\omega'}}{p}}_{\mathrm{KP}} + \underbrace{\frac{\gamma\overline{Q'_1 T'}}{\overline{T}}}_{\mathrm{PQ}}, \qquad (8)$$

where $A_T = c_{pa}\gamma(\overline{T'^2}/2\overline{T})$ is the EAPE and $\gamma = \Gamma_d/(\Gamma_d - \Gamma)$ is the inverted static stability, where Γ and Γ_d are the temperature lapse rate and dry adiabatic lapse rates, respectively; Q_1 represents the apparent heat source or total diabatic heating derived as a residual from the dry static energy budget (Nitta 1972; Yanai et al. 1973). For synoptic baroclinic disturbances in the extratropics, Q'_1 can be written as

$$Q'_1 = c_{pa}\frac{\partial T'}{\partial t} - c_{pa}(\omega'\overline{\sigma} + \overline{\omega}\sigma' + \overline{\omega'\sigma'}) + c_{pa}(\mathbf{V}'_H\cdot\nabla_H\overline{T} + \overline{\mathbf{V}}_H\cdot\nabla_H T' + \overline{\mathbf{V}'_H\cdot\nabla_H T'}), \qquad (9)$$

where $\sigma = RT/(c_{pa}p) - \partial T/\partial t = -(T/\theta)(\partial\theta/\partial p)$ is the static stability parameter (Holton 1992), R the gas constant for dry air, and c_{pa} specific heat of dry air. It should be noted that, in contrast to simplifications often made to Eq. (9) for tropical disturbances, we retained terms involving the perturbation horizontal temperature

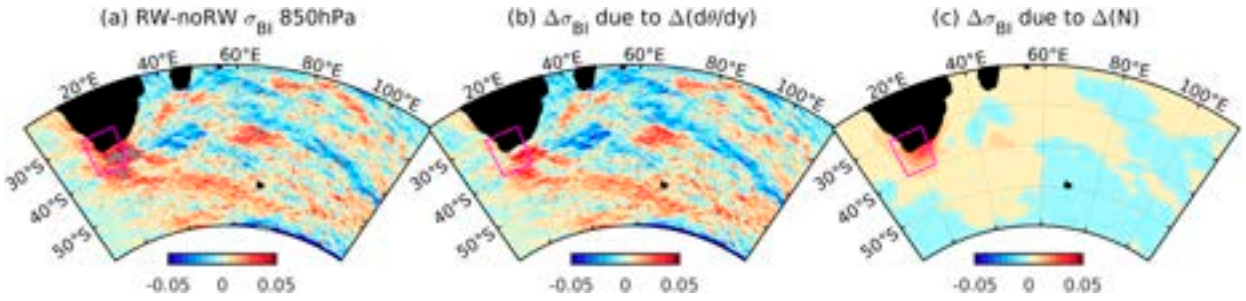

FIG. 10. (a) Annual-mean difference in $\boldsymbol{\sigma}_{\mathrm{BI}}$ at 850 hPa (day^{-1}) between RW and noRW, and the differences (b) due to meridional temperature gradient only and (c) due to change in static stability only.

gradient, vertical advection by mean vertical motion, and the products of perturbation terms.

The first two terms on the RHS of Eq. (8) represent the primary mechanisms for the generation of baroclinic transient eddies (Blackmon et al. 1977; Cai et al. 2007). The first term, called PI, is positive when the eddy heat flux is in the direction of the mean temperature gradient. That is, when positive, the baroclinic eddies relax the equatorward

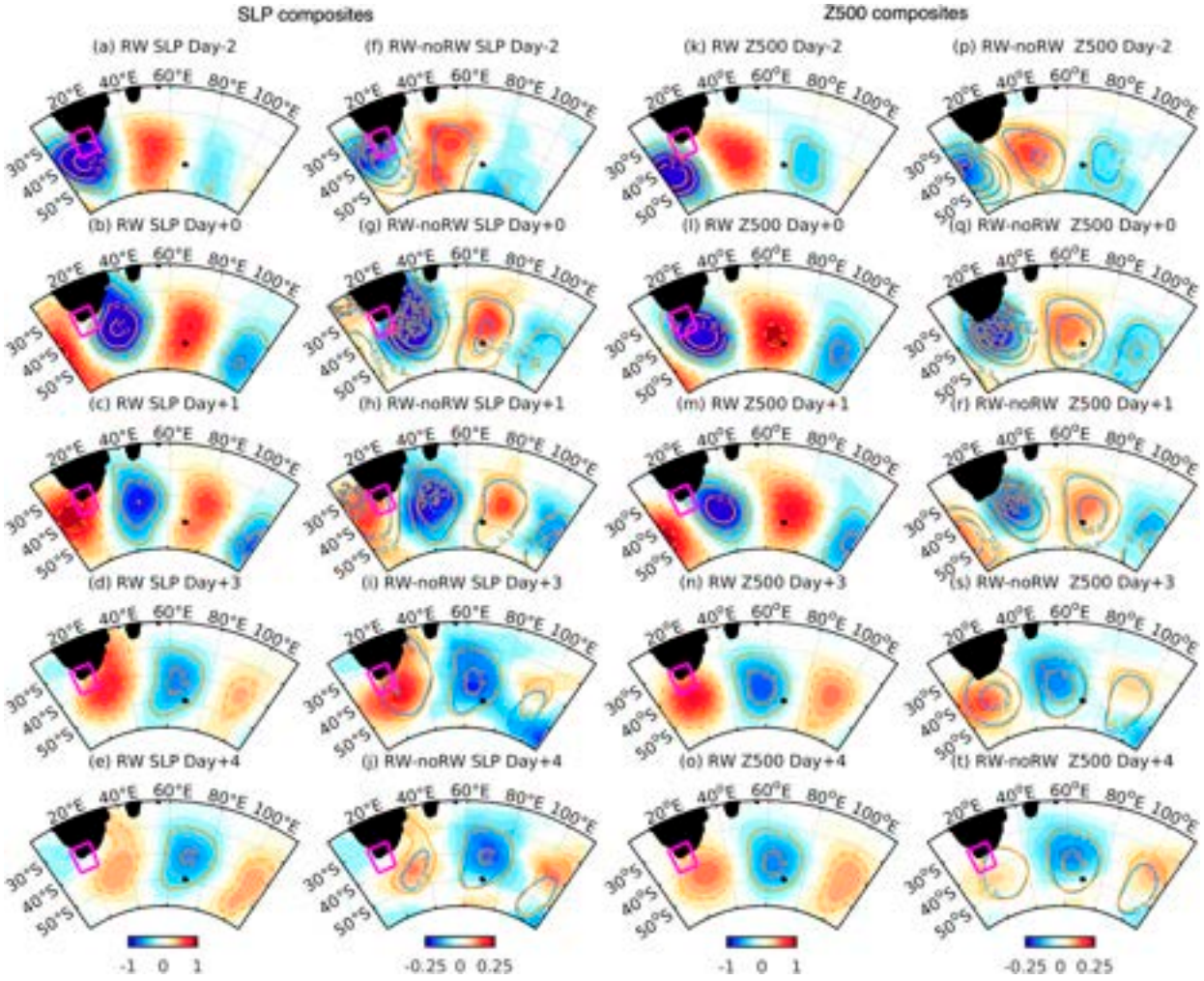

FIG. 11. Lagged composite evolution of the synoptic-scale disturbances associated with the high-THF events in the Agulhas retroflection (magenta box): (a)–(j) SLP (hPa) and (k)–(t) Z500 (gpm). Shading in the second and fourth columns show the RW − noRW with the superposed contours denoting the values from RW (orange) and noRW (blue).

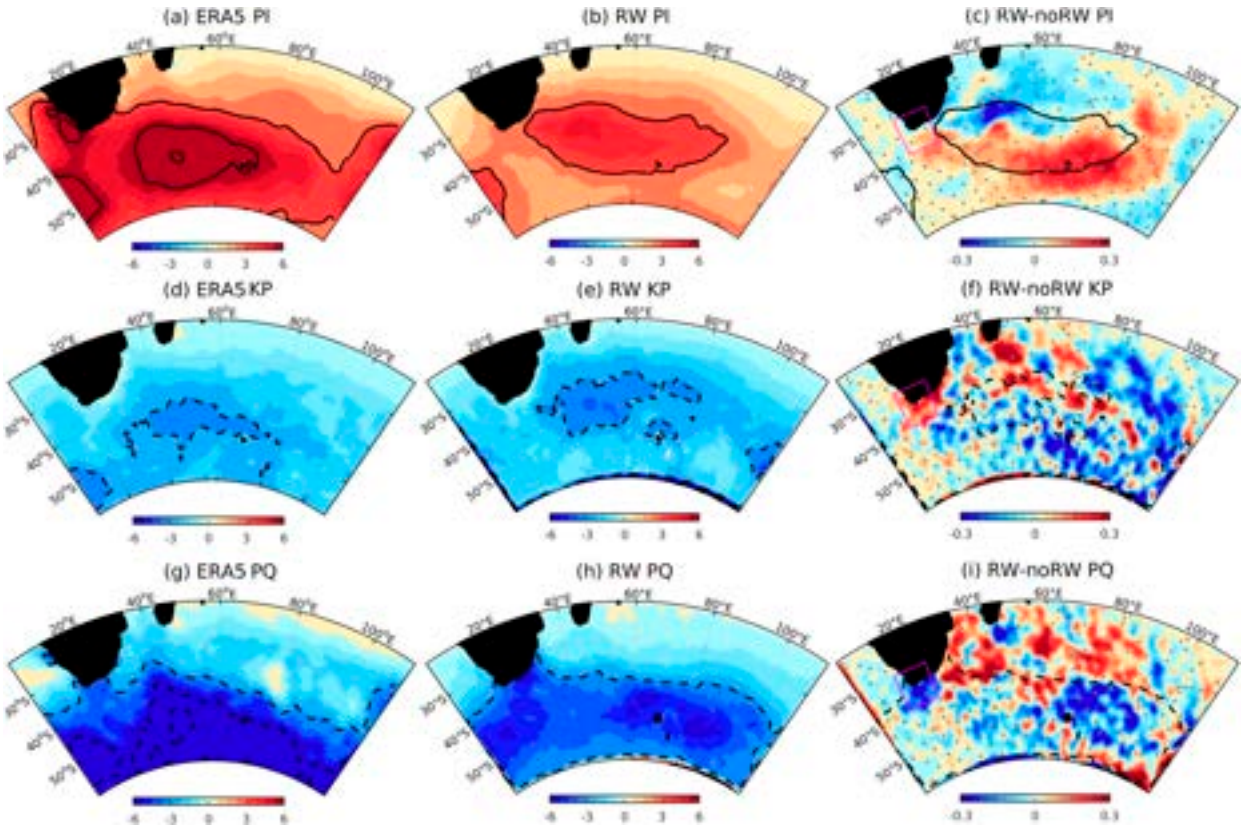

FIG. 12. Annual-mean EAPE budget terms ($10^{-4}\,m^2\,s^{-3}$) in Eq. (8): (a)–(c) baroclinic conversion from MAPE to EAPE (PI), (d)–(f) baroclinic conversion from EAPE to EKE (KP), and (g)–(i) diabatic generation/dissipation of EAPE (PQ) from (left) ERA5, (middle) RW, and (right) RW − noRW.

temperature gradient, and in this process, it converts the mean available potential energy (MAPE) to EAPE. Hence, the positive PI is a source of EAPE. The second term, KP, represents the conversion from EAPE to EKE in association with the rising (sinking) motion of the cold (warm) air parcels; that is, the negative KP is a sink of EAPE. The last term, PQ, is determined by the covariance between perturbation diabatic heating rate (Q_1') and perturbation temperature (T') (Lorenz 1955), which refers to diabatic generation or dissipation of EAPE. EAPE is generated by raising the center of mass when the perturbation heating (cooling) acts upon the anomalously warm (cooler) airmass (Oort and Peixoto 1974); conversely, EAPE is dissipated when the perturbation heating (cooling) is applied to the anomalously colder (warmer) airmass (Swanson and Pierrehumbert 1997; Branscome et al. 1989; Chang et al. 2002). For synoptic-scale weather systems advecting the cold air mass over the warm Agulhas, we expect the EAPE dissipation by PQ to be dominant.

Figure 12 shows the pressure-weighted vertical averages (1000–300 hPa) of PI, KP, and PQ from ERA5 and RW and the differences between RW and noRW. The EAPE tendency, the LHS of the Eq. (8), is small and thus not shown. Because the budget is approximately closed, estimating the PQ term as a residual from the EAPE budget yields a similar result. Figure 13 shows the changes in the respective terms in the pressure–latitude section across the Agulhas retroflection. Both ERA5 and RW indicate that, on synoptic time scales, the baroclinic conversion of MAPE to EAPE (PI) is primarily balanced by the diabatic dissipation of EAPE (PQ) and, to a lesser extent, by the conversion of EAPE to EKE (−KP). All three terms show the spatial patterns that broadly resemble the annual-mean $|\boldsymbol{\sigma}_{\mathrm{BI}}|$ and $\overline{v'T'}$ in RW, in that the maxima in energy conversion, loss, or production are spatially congruent with the maxima in low-level baroclinicity and baroclinic wave amplitude (Fig. 9).

The differences show the significant EAPE increase by PI in RW both in the main storm track and the secondary baroclinicity zone extending from the Agulhas retroflection. This increase facilitates the baroclinic conversion from EAPE to EKE (−KP), resulting in EKE increase. The PQ change is negative in the Agulhas retroflection, confirming that the enhanced diabatic EAPE damping by THF heating. From the vertical cross sections of these terms, one can see that the baroclinic conversion of the MAPE to EAPE (PI) is rooted in the lower troposphere below 700 hPa near the southern tip of Africa, where the maximum increase in PI is also found between RW and noRW. Hence, the strengthening of the low-tropospheric baroclinicity facilitates the extraction of MAPE to support the baroclinic eddy activity. PQ is strongly negative at low levels, since this

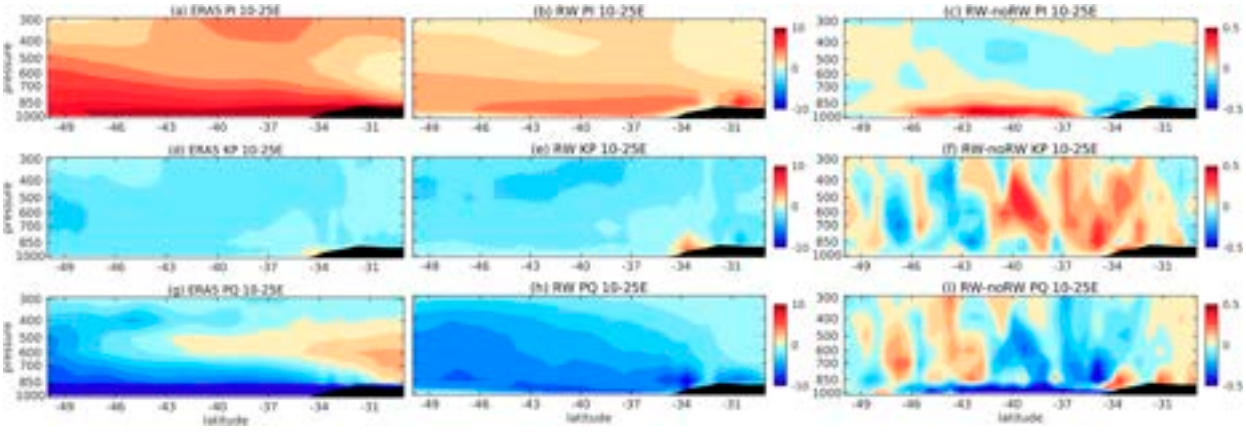

FIG. 13. As in Fig. 12, but showing the latitude–pressure section averaged over 10°–25°E.

process dampens perturbation air temperature anomalies induced by the SST and THF anomalies.

The diabatic heating term, PQ, deserves some attention. PQ includes three separate processes: latent heating due to large-scale condensation aloft, net radiative heating, and sensible and latent heating at the sea surface. The deep tropospheric heating by large-scale condensation is at its maximum along the time-mean storm track (Hoskins and Valdes 1990), with the exceptionally strong moisture and heat supply in both the warm sector of extratropical cyclones over warm currents (Emanuel et al. 1987; Czaja and Blunt 2011; Booth et al. 2012; Sheldon et al. 2017; Parfitt and Seo 2018) and the cold conveyor belt north of the cyclone center (Vannière et al. 2017; Hirata and Nonaka 2021). The descending motion under cloud-free conditions outside the storm systems leads to radiative cooling, albeit relatively small (Chang et al. 2002). Finally, the surface THF over the ocean tends to dissipate the EAPE when considering transient eddies because of the aforementioned negative covariance between Q_1' and T'. Hence, the EAPE tendency is determined by the balance between the production by condensational heating and the dissipation by the THF heating. Consistent with previous studies for the Northern Hemisphere (Ulbrich and Speth 1991; Chang et al. 2002), the total diabatic generation of EAPE by transient eddies is largely negative both in ERA5 and RW. The strongest damping of synoptic eddy temperature variance occurs in the higher latitudes near and south of the main storm track south of 40°S, but there is also locally enhanced diabatic destruction of EAPE over the Agulhas retroflection.

An alternative way to illustrate this diabatic damping of transient eddy energy by THF is to examine the so-called FT index, defined by (Marcheggiani and Ambaum 2020) as the spatial covariance between perturbation 850-hPa temperature (T') and sensible heat flux (F'), that is, $F'^*T'^*$, where asterisks (primes) denote spatial (temporal) anomalies. Over the northwestern Atlantic in boreal winter, the time-mean covariance is negative and peaks over the maximum surface flux variance near the Gulf Stream, indicative of the damping of transient eddy energy by surface fluxes. Figure 14 shows the annual-mean covariance $\overline{F'^*T'^*}$ calculated from the ERA5 and the two model simulations, where the spatial anomaly is defined with respect to the whole model domain and time anomaly defined as 2–8-day bandpass-filtered anomalies. To be consistent with the preceding analysis, here we use THF instead of sensible heat flux, although the result does not change with the use of either latent or sensible heat flux or their sum. The result shows that indeed $\overline{F'^*T'^*}$ is negative everywhere, with the maximum negative in the main storm track and the secondary maximum off South Africa. The model simulations agree very well with the ERA5, while the difference indicates that the enhanced synoptic disturbances in RW also experience enhanced diabatic damping by surface fluxes.

In summary, the transient eddy energy is enhanced by the RW primarily through the baroclinic processes associated with the increased tropospheric temperature gradients and reduced static stability, which convert potential energy from the basic

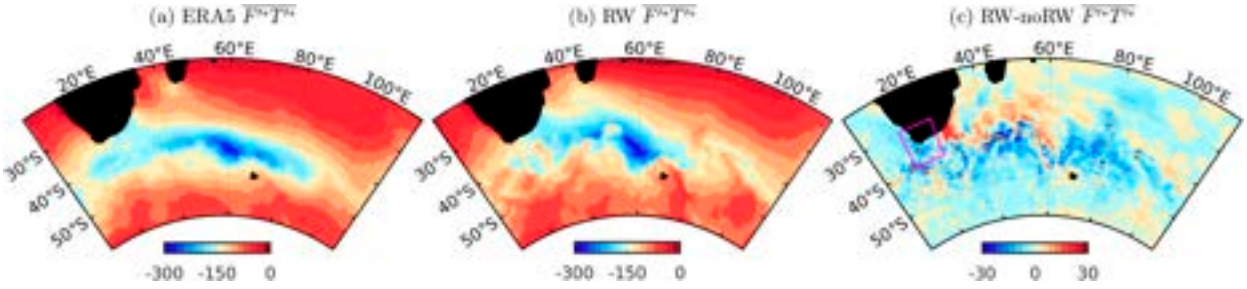

FIG. 14. Annual-mean $\overline{F'^*T'^*}$ from (a) ERA5, (b) RW, and (c) RW-noRW.

state to potential energy of transient baroclinic eddies. This production of EAPE is partially offset by the diabatic destruction of EAPE dominated by the surface fluxes. Yet, the former process wins out, and ultimately the excess net EAPE by the baroclinic processes is converted to EKE to energize storm activity.

6. Conclusions and discussion

This study investigated the sensitivity of the ocean and atmospheric circulation to including the relative wind (RW) effect in coupled ocean–atmosphere simulations in the south Indian Ocean. The main result is that, by increasing sea surface temperature (SST) and strengthening its meridional gradient in the Agulhas Current (AC) retroflection region, the RW effect results in a detectable strengthening of baroclinic eddy activity far downstream in the extratropical atmosphere. The upper-ocean circulation responses that accompany the changes in the storm track are overall consistent with previous studies documenting a significant role of the RW effect in slowing down the mean and eddy currents (Figs. 2 and 3d). The stabilized flow fields result from the reduced positive mean wind work and the increased negative eddy wind work (Figs. 5d,h), while the weakened diabatic damping of eddy potential energy by the surface fluxes (Fig. 5l) is unlikely to account for the decrease in geostrophic eddy energy with the RW effect.

A unique consequence of the stabilized ocean flow fields is that the overly energetic anticyclonic standing eddy, the biased feature ascribed to upstream retroflection of the AC without the RW effect, is considerably weakened with the RW effect (Fig. 3h). This opens a pathway through which the AC transports the warm and salty water mass of subtropical origin poleward of South Africa, resulting in two significant upper-ocean responses in the Agulhas retroflection: the warming of 1–2 K (Fig. 3l) accompanied by the increased upward turbulent heat flux (THF) (Fig. 3p) and an increased SST gradient near the subtropical front off South Africa (Fig. 6). The SST warming of 1–2 K in the Agulhas retroflection exceeds the interannual SST variability simulated by the model in the region, suggesting the significance of the RW effect on the SST responses.

The upper-ocean heat budget analysis (Figs. 7 and 8) confirms that it is the increased oceanic heat flux convergence, due in large part to the stronger (eddy) meridional temperature advection, that maintains the local surface warming against enhanced surface heat loss. The meridional SST gradient in the Agulhas retroflection is increased by the net ocean heat flux convergence with the RW effect, which, according to the theory of linear baroclinic instability that relates the growth rate of the eddies to low-level baroclinicity, would enhance the growth of midlatitude baroclinic waves in the atmosphere. Hence, the remaining question is if the thermodynamic (warmer SST) and dynamic (stronger SST gradient) changes in the Agulhas retroflection are accompanied by a consistent and robust change in baroclinic wave activity in the atmosphere.

The answer seems to be yes. As measured by various variance-based and surface-wind-based Eulerian storm track diagnostics, the present study finds increased storm activity not just locally but also along the main storm track far downstream (Fig. 9). However, the magnitude of the response is moderate, largely in the 5%–10% range of the mean. The storm track response mechanisms involve increased lower-tropospheric temperature gradients and weakened static stability, each of which contributes nearly equally to the enhanced baroclinicity over the Agulhas retroflection (Fig. 10). Our future work will include evaluating the changes in cyclone tracks and intensities in a Lagrangian perspective using multiple algorithms (Booth et al. 2017a; Zhang et al. 2019).

The downstream storm track changes are interpreted as a response forced by SST and its spatial gradients in the Agulhas retroflection. The local changes in oceans and storm track at 30°–40°S, 15°–25°E are located upstream of, and reasonably well separated from, the main storm track farther south (40°–50°S) and east (40°–60°E) (Figs. 9d–e). Nevertheless, given the robust connectivity of storm tracks upstream and downstream (Sinclair 1995), the effect of increased low-tropospheric baroclinicity in the upstream should be extended downstream. This downstream influence is confirmed by examining the composite life cycle of intense synoptic storms directly attuned to the high-THF events (Fig. 11). The result shows the robust deepening of the composite storm center, both at the surface and the midtroposphere, throughout the life cycle after the peak of the high-THF events. Finally, the energetics calculation of synoptic baroclinic waves (Figs. 12 and 13) adds that the baroclinic energy conversion from the basic flow is the chief source of the increased eddy available potential energy (EAPE), which is subsequently tapped to eddy kinetic energy. This net increased baroclinic energy conversion occurs despite the apparent diabatic dissipation of the EAPE by the surface fluxes (Figs. 12g–i and 14).

In a sense, it is hardly surprising to find that the storm track responds to changes in ocean circulation and SST brought about by the RW effect. On the one hand, studies based on reanalyses and atmospheric model simulations have convincingly demonstrated an impact of the so-called frontal-scale (thermal) air–sea interaction over the WBCs, where the variability and intensity of extratropical storm track are strongly influenced by their thermal coupling with SSTs mediated by the WBCs (Small et al. 2014; Parfitt and Czaja 2016; O'Reilly and Czaja 2015; Ma et al. 2015a). For the AC case, Reason (2001) found that the responses in the extratropical cyclone activity to the AC SST reaching as far as the southeastern Australian–Tasman Sea region. The magnitude of the local perturbation SSTs varies but is in the range of 1–3 K (e.g., Reason 2001; Smirnov et al. 2015; Kuwano-Yoshida et al. 2010), with the resulting SST anomaly patterns encompassing the WBCs and their extensions (Seo et al. 2017).

On the other hand, ocean-only or high-resolution regional coupled modeling studies have demonstrated that the intensity, position, and variability of simulated ocean flow fields over both western and eastern boundary current systems are markedly improved (damped) when the mechanical air–sea interaction represented by the RW effect is taken into account. Some of these previous studies documented notable downstream effects on SST and monsoon circulation associated with shifts in boundary currents (Seo 2017). For the south Indian Ocean,

Renault et al. (2017) and the present study, both based on high-resolution regional coupled model simulations, agree that the SST warming is in the 1–2-K range and confined to the Agulhas retroflection. The magnitude of the SST anomaly is comparable to that identified in the aforementioned atmospheric modeling studies.

Therefore, it seems clear that the mechanical and thermal air–sea interactions are inherently and inextricably linked together over the Agulhas retroflection to influence the extratropical storm tracks. This implies that improved understanding and simulation of the extratropical storm tracks in this region and possibly other WBCs in numerical models requires an accurate representation of the air–sea momentum exchange associated with the ocean currents and its indirect rectifying impacts on the atmosphere. The demonstrated local and downstream impacts of surface currents on the storm track via surface fluxes and diabatic feedback processes also provide a possible application of high-resolution satellite observations of collocated vector wind and surface currents from the proposed Doppler scatterometer Winds and Currents Mission (WaCM; Bourassa et al. 2016).

Although this study adopted an unusually large model domain for regional coupled model simulations, the simulated storm track far downstream would be affected by the prescribed boundary conditions. Hence, a more robust conclusion on the RW effect on the extratropical storm track would require additional modeling approaches, including one that affords long-term or multi-ensemble simulations and encompasses a much larger, possibly global, domain. This presents significant computational challenges, in that the RW effect is known to be highly scale dependent (Renault et al. 2018; Jullien et al. 2020; Fig. 4b). That is, the stabilization of the oceanic flow fields by the RW effect is most effective at a length scale equivalent to the Rossby internal deformation radius (Fig. 2b; Seo et al. 2019). This implies a stringent resolution criterion for global coupled models to fully represent ocean mesoscale processes and the induced mechanical and thermal (diabatic) interactions with the atmosphere to more robustly evaluate their indirect impacts on the far-field atmospheric circulation. This is an active research area (e.g., Moreton et al. 2020; Siqueira et al. 2021).

Another important caveat of the study is the lack of wind response to the current feedback. Since the RW effect is treated outside of the atmospheric surface-layer scheme, the current study does not capture the partial re-energization effect due to the direct low-level wind response to ocean mesoscale currents (Renault et al. 2016, 2017, 2019). Thus, the difference in eddy damping between the present study and Renault et al. (2017) is likely attributed to this lack of direct wind response to ocean current.

Finally, the present simulations exhibit some biases in the Agulhas retroflection, even with the RW effect. The simulated AC is more variable, and the THF maximum is displaced far eastward compared to the observational products. This indicates that other aspects of the Agulhas system dynamics are not reliably simulated, possibly including the triggering of Natal pulses over the Mozambique Channel (Biastoch et al. 2008; Renault et al. 2017). The biases in SST and THF would also likely impact the sensitivity of the storm track (Lee et al. 2018). However, the mean state biases are inevitable in climate models, particularly in this energetic region where a mean is not well defined or constrained. Despite the lingering biases, the results demonstrate that the improved representation of air–sea momentum exchanges results in various improvements in the coupled model (Renault et al. 2017; Fox-Kemper et al. 2019), bringing the model simulation one step closer to the observationally informed products. Dedicated sensitivity experiments are needed to quantify the impacts of the bias; this is beyond the scope of the present work.

Acknowledgments. Seo acknowledges the support from the NSF (OCE-2022846), NOAA (NA19OAR4310376), ONR (N00014-17-12398), and the Andrew W. Mellon Foundation Endowed Fund for Innovative Research at Woods Hole Oceanographic Institution (WHOI). Song is supported by the National Research Foundation of Korea (NRF) grant funded by the Korea government (MSIT) (NRF-2019R1C1C1003663). O'Neill was supported by the NASA Grants 80NSSC19K1117 and 80NSSC19K1011. The computing resources were provided by the WHOI High-Performance Computing Facility. Comments on the manuscript by J. Small are appreciated. The authors thank two anonymous reviewers and Dr. Lionel Renault for their constructive comments, which helped to substantially improve the manuscript.

REFERENCES

Biastoch, A. C., J. Lutjeharms, C. W. Böning, and M. Scheinert, 2008: Mesoscale perturbations control inter-ocean exchange south of Africa. *Geophys. Res. Lett.*, **35**, L20602, https://doi.org/10.1029/2008GL035132.

Bishop, S. P., R. J. Small, F. O. Bryan, and R. A. Tomas, 2017: Scale dependence of mid–latitude air–sea interaction. *J. Climate*, **30**, 8207–8221, https://doi.org/10.1175/JCLI-D-17-0159.1.

——, ——, and ——, 2020: The global sink of available potential energy by mesoscale air–sea interaction. *J. Adv. Model. Earth Syst.*, **12**, e2020MS002118, https://doi.org/10.1029/2020MS002118.

Blackmon, M. L., J. M. Wallace, N.-C. Lau, and S. L. Mullen, 1977: An observational study of the Northern Hemisphere wintertime circulation. *J. Atmos. Sci.*, **34**, 1040–1053, https://doi.org/10.1175/1520-0469(1977)034<1040:AOSOTN>2.0.CO;2.

Booth, J. F., L. Thompson, J. Patoux, K. A. Kelly, and S. Dickinson, 2010: The signature of midlatitude tropospheric storm tracks in the surface winds. *J. Climate*, **23**, 1160–1174, https://doi.org/10.1175/2009JCLI3064.1.

——, ——, ——, and ——, 2012: Sensitivity of midlatitude storm intensification to perturbations in the sea surface temperature near the Gulf Stream. *Mon. Wea. Rev.*, **140**, 1241–1256, https://doi.org/10.1175/MWR-D-11-00195.1.

——, E. Dunn-Sigouin, and S. Pfahl, 2017a: The relationship between extratropical cyclone steering and blocking along the North American east coast. *Geophys. Res. Lett.*, **44**, 11 976–11 984, https://doi.org/10.1002/2017GL075941.

——, Y. O. Kwon, S. Ko, R. J. Small, and R. Msadek, 2017b: Spatial patterns and intensity of the surface storm tracks in CMIP5 models. *J. Climate*, **30**, 4965–4981, https://doi.org/10.1175/JCLI-D-16-0228.1.

Bourassa, M., E. Rodríguez, and D. B. Chelton, 2016: Winds and currents mission: Ability to observe mesoscale AIR/SEA coupling. *2016 IEEE Int. Geoscience and Remote Sensing Symp. (IGARSS)*, Beijing, China, IEEE, 7392–7395, https://doi.org/10.1109/IGARSS.2016.7730928.

Braby, L., B. Backeberg, M. Krug, and C. Reason, 2020: Quantifying the impact of wind-current feedback on mesoscale variability in forced simulation experiments of the Agulhas Current using an eddy-tracking algorithm. *J. Geophys. Res. Oceans*, **125**, e2019JC015365, https://doi.org/10.1029/2019JC015365.

Branscome, L. E., W. J. Gutowski, and D. A. Stewart, 1989: Effects of surface fluxes on the nonlinear development of baroclinic waves. *J. Geophys. Res.*, **46**, 460–475, https://doi.org/10.1175/1520-0469(1989)046<0460:EOSFOT>2.0.CO;2.

Brink, K. H., and H. Seo, 2016: Continental shelf baroclinic instability. Part II: Oscillating wind forcing. *J. Phys. Oceanogr.*, **46**, 569–582, https://doi.org/10.1175/JPO-D-15-0048.1.

Cai, M., S. Yang, H. M. van den Dool, and V. E. Kousky, 2007: Dynamical implications of the orientation of atmospheric eddies: A local energetics perspective. *Tellus*, **59A**, 127–140, https://doi.org/10.1111/j.1600-0870.2006.00213.x.

Carton, J.A., and B. S. Giese, 2008. A reanalysis of ocean climate using Simple Ocean Data Assimilation (SODA). *Mon. Wea. Rev.*, **136**, 2999–3017, https://doi.org/10.1175/2007MWR1978.1.

Chang, E. K. M., 1993: Downstream development of baroclinic waves as inferred from regression analysis. *J. Atmos. Sci.*, **50**, 2038–2053, https://doi.org/10.1175/1520-0469(1993)050<2038:DDOBWA>2.0.CO;2.

——, and I. Olanski, 1993: On the dynamics of a storm track. *J. Atmos. Sci.*, **50**, 999–1015, https://doi.org/10.1175/1520-0469(1993)050<0999:OTDOAS>2.0.CO;2.

——, S. Lee, and K. L. Swanson, 2002: Storm track dynamics. *J. Climate*, **15**, 2163–2183, https://doi.org/10.1175/1520-0442(2002)015<02163:STD>2.0.CO;2.

Charney, J. G., 1947: The dynamics of long waves in a baroclinic westerly current. *J. Meteor.*, **4**, 136–162, https://doi.org/10.1175/1520-0469(1947)004<0136:TDOLWI>2.0.CO;2.

Chelton, D. B., and M. G. Schlax, 2003: The accuracies of smoothed sea surface height fields constructed from tandem satellite altimeter datasets. *J. Atmos. Oceanic Technol.*, **20**, 1276–1302, https://doi.org/10.1175/1520-0426(2003)020<1276:TAOSSS>2.0.CO;2.

——, R. A. deSzoeke, and M. G. Schlax, 1998: Geographical variability of the first baroclinic Rossby radius of deformation. *J. Phys. Oceanogr.*, **28**, 433–460, https://doi.org/10.1175/1520-0485(1998)028<0433:GVOTFB>2.0.CO;2.

Chen, F., and J. Dudhia, 2001: Coupling an advanced land-surface/hydrology model with the Penn State/NCAR MM5 modeling system. Part I: Model implementation and sensitivity. *Mon. Wea. Rev.*, **129**, 569–585, https://doi.org/10.1175/1520-0493(2001)129<0569:CAALSH>2.0.CO;2.

Chou, M.-D., and M. J. Suarez, 1999: A solar radiation parameterization for atmospheric studies. Tech. Memo. NASA/TM-1999-104606, Vol. 15, 38 pp., http://gmao.gsfc.nasa.gov/pubs/docs/Chou136.pdf.

Czaja, A., and N. Blunt, 2011: A new mechanism for ocean–atmosphere coupling in midlatitudes. *Quart. J. Roy. Meteor. Soc.*, **137**, 1095–1101, https://doi.org/10.1002/qj.814.

——, C. Frankignoul, S. Minobe, and B. Vannière, 2019: Simulating the midlatitude atmospheric circulation: What might we gain from high-resolution modeling of air–sea interactions? *Curr. Climate Change Rep.*, **5**, 390–406, https://doi.org/10.1007/s40641-019-00148-5.

da Silva, A. M., C. C. Young, and S. Levitus, 1994: *Algorithms and Procedures*. Vol. 1, *Atlas of Surface Marine Data 1994*, NOAA Atlas NESDIS 6, 83 pp.

Dee, D., and Coauthors, 2011: The ERA-Interim reanalysis: Configuration and performance of the data assimilation system. *Quart. J. Roy. Meteor. Soc.*, **137**, 553–597, https://doi.org/10.1002/qj.828.

Dong, S., J. Sprintall, and S. T. Gille, 2006: Location of the polar front from AMSR-E satellite sea surface temperature measurements. *J. Phys. Oceanogr.*, **36**, 2075–2089, https://doi.org/10.1175/JPO2973.1.

Eady, E. T., 1949: Long waves and cyclone waves. *Tellus*, **1**, 33–52, https://doi.org/10.3402/tellusa.v1i3.8507.

Eden, C., and H. Dietze, 2009: Effects of mesoscale eddy/wind interactions on biological new production and eddy kinetic energy. *J. Geophys. Res.*, **114**, C05023, https://doi.org/10.1029/2008JC005129.

Edson, J. B., and Coauthors, 2013: On the exchange of momentum over the open ocean. *J. Phys. Oceanogr.*, **43**, 1589–1610, https://doi.org/10.1175/JPO-D-12-0173.1.

Emanuel, K. A., M. Fantini, and A. J. Thorpe, 1987: Baroclinic instability in an environment of small stability to slantwise moist convection. Part I: Two-dimensional models. *J. Atmos. Sci.*, **44**, 1559–1573, https://doi.org/10.1175/1520-0469(1987)044<1559:BIIAEO>2.0.CO;2.

Fairall, C., E. F. Bradley, J. Godfrey, G. Wick, J. Edson, and G. Young, 1996: Cool-skin and warm-layer effects on sea surface temperature. *J. Geophys. Res.*, **101**, 1295–1308, https://doi.org/10.1029/95JC03190.

——, ——, J. Hare, A. Grachev, and J. Edson, 2003: Bulk parameterization of air–sea fluxes: Updates and verification for the COARE algorithm. *J. Climate*, **16**, 571–591, https://doi.org/10.1175/1520-0442(2003)016<0571:BPOASF>2.0.CO;2.

Fox-Kemper, B., and Coauthors, 2019: Sources and sinks of ocean mesoscale eddy energy: A joint US CLIVAR and CLIVAR Workshop Rep., 2019-5, 21 pp., https://doi.org/10.5065/CH5R-5034.

Haidvogel, D. B., H. G. Arango, K. Hedstrom, A. Beckmann, P. Malanotte-Rizzoli, and A. F. Shchepetkin, 2000: Model evaluation experiments in the North Atlantic Basin: Simulations in nonlinear terrain-following coordinates. *Dyn. Atmos. Oceans*, **32**, 239–281, https://doi.org/10.1016/S0377-0265(00)00049-X.

Hersbach, H., and Coauthors, 2020: The ERA5 global reanalysis. *Quart. J. Roy. Meteor. Soc.*, **146**, 1999–2049, https://doi.org/10.1002/qj.3803.

Hirata, H., and M. Nonaka, 2021: Impacts of strong warm ocean currents on development of extratropical cyclones through the warm and cold conveyor belts: A review. *Tropical and Extratropical Air–Sea Interactions*, Elsevier, 267–293, http://www.sciencedirect.com/science/article/pii/B9780128181560000149.

Holton, J. R., 1992: *An Introduction to Dynamic Meteorology*. 3rd ed. Academic Press, 511 pp.

Hong, S.-Y., and J.-O. Lim, 2006: The WRF single-moment 6-class microphysics scheme (WSM6). *J. Korean Meteor. Soc.*, **42**, 129–151.

——, Y. Noh, and J. Dudhia, 2006: A new vertical diffusion package with an explicit treatment of entrainment processes. *Mon. Wea. Rev.*, **134**, 2318–2341, https://doi.org/10.1175/MWR3199.1.

Hoskins, B. J., and P. J. Valdes, 1990: On the existence of storm tracks. *J. Atmos. Sci.*, **47**, 1854–1864, https://doi.org/10.1175/1520-0469(1990)047<1854:OTEOST>2.0.CO;2.

——, and K. I. Hodges, 2005: A new perspective on Southern Hemisphere storm tracks. *J. Climate*, **18**, 4108–4129, https://doi.org/10.1175/JCLI3570.1.

Hotta, D., and H. Nakamura, 2011: On the significance of the sensible heat supply from the ocean in the maintenance of the mean baroclinicity along storm tracks. *J. Climate*, **24**, 3377–3401, https://doi.org/10.1175/2010JCLI3910.1.

Iacono, M. J., J. S. Delamere, E. J. Mlawer, M. W. Shephard, S. A. Clough, and W. D. Collins, 2008: Radiative forcing by long-lived greenhouse gases: Calculations with the AER radiative transfer models. *J. Geophys. Res.*, **113**, D13103, https://doi.org/10.1029/2008JD009944.

Jullien, S., S. Masson, V. Oerder, G. Samson, F. Colas, and L. Renault, 2020: Impact of ocean–atmosphere current feedback on ocean mesoscale activity: Regional variations and sensitivity to model resolution. *J. Climate*, **33**, 2585–2602, https://doi.org/10.1175/JCLI-D-19-0484.1.

Jury, M. R., and S. Courtney, 1991: A transition in weather over the Agulhas Current. *S. Afr. J. Mar. Sci.*, **10**, 159–171, https://doi.org/10.2989/02577619109504629.

——, H. R. Valentine, and J. R. E. Lutjeharms, 1993: Influence of the Agulhas Current on summer rainfall along the southeast coast of South Africa. *J. Appl. Meteor.*, **32**, 1282–1287, https://doi.org/10.1175/1520-0450(1993)032<1282:IOTACO>2.0.CO;2.

Kuwano-Yoshida, A., and S. Minobe, 2017: Storm track response to SST fronts in the northwestern Pacific region in an AGCM. *J. Climate*, **30**, 1081–1102, https://doi.org/10.1175/JCLI-D-16-0331.1.

——, ——, and S.-P. Xie, 2010: Precipitation response to the Gulf Stream in an atmospheric GCM. *J. Climate*, **23**, 3676–3698, https://doi.org/10.1175/2010JCLI3261.1.

Large, W. G., J. C. McWilliams, and S. C. Doney, 1994: Oceanic vertical mixing: A review and a model with a nonlocal boundary layer parameterization. *Rev. Geophys.*, **32**, 363–403, https://doi.org/10.1029/94RG01872.

Lau, K.-H., and N.-C. Lau, 1992: The energetics and propagation dynamics of tropical summertime synoptic-scale disturbances. *J. Climate*, **120**, 2523–2539, https://doi.org/10.1175/1520-0493(1992)120<2523:TEAPDO>2.0.CO;2.

Lee, R. W., T. J. Woollings, B. J. Hoskins, K. D. Williams, C. H. O'Reilly, and G. Masato, 2018: Impact of Gulf Stream SST biases on the global atmospheric circulation. *Climate Dyn.*, **51**, 3369–3387, https://doi.org/10.1007/s00382-018-4083-9.

Lindzen, R. S., and B. J. Farrell, 1980: A simple approximate result for the maximum growth rate of baroclinic instabilities. *J. Atmos. Sci.*, **37**, 1648–1654, https://doi.org/10.1175/1520-0469(1980)037<1648:ASARFT>2.0.CO;2.

Liu, W. T., X. Xie, and P. P. Niiler, 2007: Ocean–atmosphere interaction over Agulhas Extension meanders. *J. Climate*, **20**, 5784–5797, https://doi.org/10.1175/2007JCLI1732.1.

Lorenz, E. N., 1955: Available potential energy and the maintenance of the general circulation. *Tellus*, **7**, 157–167, https://doi.org/10.3402/tellusa.v7i2.8796.

Luo, J.-J., S. Masson, E. R. G. Madec, and T. Yamagata, 2005: Reducing climatology bias in an ocean–atmosphere CGCM with improved coupling physics. *J. Climate*, **18**, 2344–2360, https://doi.org/10.1175/JCLI3404.1.

Lutjeharms, J. R. E., and R. C. van Ballegooyen, 1984: Topographic control in the Agulhas Current system. *Deep-Sea Res.*, **31A**, 1321–1337, https://doi.org/10.1016/0198-0149(84)90004-9.

——, and H. R. Roberts, 1988: The Natal pulse: An extreme transient of the Agulhas Current. *J. Geophys. Res.*, **93**, 631–645, https://doi.org/10.1029/JC093iC01p00631.

——, and R. C. van Ballegooyen, 1988: Anomalous upstream retroflection in the Agulhas Current. *Science*, **240**, 1770, https://doi.org/10.1126/science.240.4860.1770.

Ma, X., P. Chang, R. Saravanan, R. M. J.-S. Hseih, D. Wu, X. Lin, L. Wu, and Z. Jing, 2015a: Distant influence of Kuroshio eddies on North Pacific weather patterns. *Sci. Rep.*, **5**, 17785, https://doi.org/10.1038/srep17785.

——, ——, ——, D. Wu, X. Lin, L. Wu, and X. Wan, 2015b: Winter extreme flux events in the Kuroshio and Gulf Stream Extension regions and relationship with modes of North Pacific and Atlantic variability. *J. Climate*, **28**, 4950–4970, https://doi.org/10.1175/JCLI-D-14-00642.1.

——, and Coauthors, 2016: Western boundary currents regulated by interaction between ocean eddies and the atmosphere. *Nature*, **535**, 533–537, https://doi.org/10.1038/nature18640.

Marcheggiani, A., and M. H. P. Ambaum, 2020: The role of heat-flux–temperature covariance in the evolution of weather system. *Wea. Climate Dyn.*, **1**, 701–713, https://doi.org/10.5194/wcd-1-701-2020.

Mason, S. J., 1995: Sea-surface temperature–South African rainfall associations, 1910–1989. *Int. J. Climatol.*, **15**, 119–135, https://doi.org/10.1002/joc.3370150202.

Messager, C., and S. Swart, 2016: Significant atmospheric boundary layer change observed above an Agulhas Current warm core eddy. *Adv. Meteor.*, **2016**, 3659657, https://doi.org/10.1155/2016/3659657.

Moisan, J. R., and P. P. Niiler, 1998: The seasonal heat budget of the North Pacific: Net heat flux and heat storage rates (1950–1990). *J. Phys. Oceanogr.*, **28**, 401–421, https://doi.org/10.1175/1520-0485(1998)028<0401:TSHBOT>2.0.CO;2.

Moreton, S. M., D. Ferreira., M. J. Roberts, and H. T. Hewitt, 2020: Evaluating surface eddy properties in coupled climate simulations with 'eddy-present' and 'eddy-rich' ocean resolution. *Ocean. Modell.*, **147**, 101567, https://doi.org/10.1016/j.ocemod.2020.101567.

Nakamura, H., and A. Shimpo, 2004: Seasonal variations in the Southern Hemisphere storm tracks and jet streams as revealed in a reanalysis dataset. *J. Climate*, **17**, 1828–1844, https://doi.org/10.1175/1520-0442(2004)017<1828:SVITSH>2.0.CO;2.

——, M. Nakamura, and J. L. Anderson, 1997: The role of high- and low-frequency dynamics and blocking formation. *Mon. Wea. Rev.*, **125**, 2074–2093, https://doi.org/10.1175/1520-0493(1997)125<2074:TROHAL>2.0.CO;2.

——, T. Sampe, Y. Tanimoto, and A. Shimpo, 2004: Observed associations among storm tracks, jet streams and midlatitude oceanic fronts. *Earth's Climate: The Ocean–Atmosphere Interaction, Geophys. Monogr.*, Vol. 147, Amer. Geophys. Union, 329–346.

——, ——, A. Goto, W. Ohfuchi, and S.-P. Xie, 2008: On the importance of midlatitude oceanic frontal zones for the mean state and dominant variability in the tropospheric circulation. *Geophys. Res. Lett.*, **35**, L15709, https://doi.org/10.1029/2008GL034010.

Nitta, T., 1972: Energy budget of wave disturbances over the Marshall Islands during years of 1956 and 1958. *J. Meteor. Soc. Japan*, **50**, 71–84, https://doi.org/10.2151/jmsj1965.50.2_71.

Nkwinkwa Njouodo, A. S., S. Koseki, N. Keenlyside, and M. Rouault, 2018: Atmospheric signature of the Agulhas Current. *Geophys. Res. Lett.*, **45**, 5185–5193, https://doi.org/10.1029/2018GL077042.

O'Neill, L. W., D. B. Chelton, and S. K. Esbensen, 2003: Observations of SST-induced perturbations of the wind stress field over the Southern Ocean on seasonal timescales. *J. Climate*, **16**, 2340–2354, https://doi.org/10.1175/2780.1.

——, ——, ——, and F. J. Wentz, 2005: High-resolution satellite measurements of the atmospheric boundary layer response to SST variations along the Agulhas Return Current. *J. Climate*, **18**, 2706–2723, https://doi.org/10.1175/JCLI3415.1.

——, T. Haack, D. B. Chelton, and E. Skyllingstad, 2017: The Gulf Stream convergence zone in the time-mean winds. *J. Climate*, **74**, 2383–2412, https://doi.org/10.1175/JAS-D-16-0213.1.

Oort, A. H., and J. P. Peixoto, 1974: The annual cycle of the energetics of the atmosphere on a planetary scale. *J. Geophys. Res.*, **79**, 2705–2719, https://doi.org/10.1029/JC079i018p02705.

O'Reilly, C. H., and A. Czaja, 2015: The response of the Pacific storm track and atmospheric circulation to Kuroshio Extension variability. *Quart. J. Roy. Meteor. Soc.*, **141**, 52–66, https://doi.org/10.1002/qj.2334.

Pacanowski, R. C., 1987: Effect of equatorial currents on surface stress. *J. Phys. Oceanogr.*, **17**, 833–838, https://doi.org/10.1175/1520-0485(1987)017<0833:EOECOS>2.0.CO;2.

Parfitt, R., and A. Czaja, 2016: On the contribution of synoptic transients to the mean atmospheric state in the Gulf Stream region. *Quart. J. Roy. Meteor. Soc.*, **142**, 1554–1561, https://doi.org/10.1002/qj.2689.

——, and H. Seo, 2018: A new framework for near-surface wind convergence over the Kuroshio Extension and Gulf Stream in wintertime: The role of atmospheric fronts. *Geophys. Res. Lett.*, **45**, 9909–9918, https://doi.org/10.1029/2018GL080135.

Perlin, N. S., P. de Szoeke, D. B. Chelton, R. M. Samelson, E. D. Skyllingstad, and L. W. O'Neill, 2014: Modeling the atmospheric boundary layer wind response to mesoscale sea surface temperature perturbations. *Mon. Wea. Rev.*, **142**, 4284–4307, https://doi.org/10.1175/MWR-D-13-00332.1.

——, I. Kamenkovich, Y. Gao, and B. P. Kirtman, 2020: A study of mesoscale air–sea interaction in the Southern Ocean with a regional coupled model. *Ocean Modell.*, **153**, 101660, https://doi.org/10.1016/j.ocemod.2020.101660.

Reason, C. J. C., 2001: Evidence for the influence of the Agulhas Current on regional atmospheric circulation patterns. *J. Climate*, **14**, 2769–2778, https://doi.org/10.1175/1520-0442(2001)014<2769:EFTIOT>2.0.CO;2.

——, and H. M. Mulenga, 1999: Relationships between South African rainfall and SST anomalies in the southwest Indian Ocean. *Int. J. Climatol.*, **19**, 1651–1673, https://doi.org/10.1002/(SICI)1097-0088(199912)19:15<1651::AID-JOC439>3.0.CO;2-U.

Renault, L., M. J. Molemaker, J. Gula, S. Masson, and J. C. McWilliams, 2016: Control and stabilization of the Gulf Stream by oceanic current interaction with the atmosphere. *J. Phys. Oceanogr.*, **46**, 3439–3453, https://doi.org/10.1175/JPO-D-16-0115.1.

——, J. C. McWilliams, and P. Penven, 2017: Modulation of the Agulhas Current retroflection and leakage by oceanic current interaction with the atmosphere in coupled simulations. *J. Phys. Oceanogr.*, **47**, 2077–2100, https://doi.org/10.1175/JPO-D-16-0168.1.

——, ——, and J. Gula, 2018: Dampening of submesoscale currents by air–sea stress coupling in the Californian upwelling system. *Sci. Rep.*, **8**, 13388, https://doi.org/10.1038/s41598-018-31602-3.

——, P. Marchesiellio, S. Masson, and J. C. McWilliams, 2019: Remarkable control of western boundary currents by eddy killing, a mechanical air–sea coupling process. *Geophys. Res. Lett.*, **46**, 2743–2751, https://doi.org/10.1029/2018GL081211.

Reynolds, R. W., T. M. Smith, C. Liu, D. B. Chelton, K. S. Casey, and M. G. Schlax, 2007: Daily high-resolution-blended analyses for sea surface temperature. *J. Climate*, **20**, 5473–5496, https://doi.org/10.1175/2007JCLI1824.1.

Roberts, C. D., M. D. Palmer, D. G. D. R. P. Allan, P. P. Hyder, C. Liu, and D. Smith, 2017: Surface flux and ocean heat transport convergence contributions to seasonal and interannual variations of ocean heat content. *J. Geophys. Res. Oceans*, **122**, 726–744, https://doi.org/10.1002/2016JC012278.

Rouault, M., and P. Penven, 2011: New perspectives on Natal pulses from satellite observations. *J. Geophys. Res.*, **116**, C07013, https://doi.org/10.1029/2010JC006866.

——, A. M. Lee-Thorp, and J. R. E. Lutjeharms, 2000: Observations of the atmospheric boundary layer above the Agulhas Current during alongcurrent winds. *J. Phys. Oceanogr.*, **30**, 40–50, https://doi.org/10.1175/1520-0485(2000)030<0040:TABLAT>2.0.CO;2.

Sampe, T., and S.-P. Xie, 2007: Mapping high sea winds from space: A global climatology. *Bull. Amer. Meteor. Soc.*, **88**, 1965–1978, https://doi.org/10.1175/BAMS-88-12-1965.

Seo, H., 2017: Distinct influence of air–sea interactions mediated by mesoscale sea surface temperature and surface current in the Arabian Sea. *J. Climate*, **30**, 8061–8080, https://doi.org/10.1175/JCLI-D-16-0834.1.

——, A. J. Miller, and J. O. Roads, 2007: The Scripps Coupled Ocean–Atmosphere Regional (SCOAR) model, with applications in the eastern Pacific sector. *J. Climate*, **20**, 381–402, https://doi.org/10.1175/JCLI4016.1.

——, A. C. Subramanian, A. J. Miller, and N. R. Cavanaugh, 2014: Coupled impacts of the diurnal cycle of sea surface temperature on the Madden–Julian oscillation. *J. Climate*, **27**, 8422–8443, https://doi.org/10.1175/JCLI-D-14-00141.1.

——, A. J. Miller, and J. R. Norris, 2016: Eddy–wind interaction in the California Current System: Dynamics and impacts. *J. Phys. Oceanogr.*, **46**, 439–459, https://doi.org/10.1175/JPO-D-15-0086.1.

——, Y.-O. Kwon, T. M. Joyce, and C. C. Ummenhofer, 2017: On the predominant nonlinear response of the extratropical atmosphere to meridional shift of the Gulf Stream. *J. Climate*, **30**, 9679–9702, https://doi.org/10.1175/JCLI-D-16-0707.1.

——, A. C. Subramanian, H. Song, and J. S. Chowdary, 2019: Coupled effects of ocean current on wind stress in the Bay of Bengal: Eddy energetics and upper ocean stratification. *Deep-Sea Res. II*, **168**, 104617, https://doi.org/10.1016/j.dsr2.2019.07.005.

Shchepetkin, A. F., and J. C. McWilliams, 2005: The Regional Oceanic Modeling System (ROMS): A split-explicit, free-surface, topography-following-coordinate ocean model. *Ocean Modell.*, **9**, 347–404, https://doi.org/10.1016/j.ocemod.2004.08.002.

Sheldon, L., A. Czaja, B. Vannière, C. Morcrette, B. Sohet, M. Casado, and D. Smith, 2017: A warm path to Gulf Stream–troposphere interactions. *Tellus*, **69A**, 1–13, https://doi.org/10.1080/16000870.2017.1299397.

Sinclair, M. R., 1995: A climatology of cyclogenesis for the Southern Hemisphere. *Mon. Wea. Rev.*, **123**, 1601–1619, https://doi.org/10.1175/1520-0493(1995)123<1601:ACOCFT>2.0.CO;2.

——, J. A. Renwick, and J. W. Kidson, 1997: Low-frequency variability of Southern Hemisphere sea level pressure and weather system activity. *Mon. Wea. Rev.*, **125**, 2531–2543, https://doi.org/10.1175/1520-0493(1997)125<2531:LFVOSH>2.0.CO;2.

Singleton, A. T., and C. J. C. Reason, 2006: Numerical simulations of a severe rainfall event over the Eastern Cape coast of South Africa: Sensitivity to sea surface temperature and topography. *Tellus*, **58A**, 335–367, https://doi.org/10.1111/j.1600-0870.2006.00180.x.

Siqueira, L., B. P. Kirtman, and L. C. Laurindo, 2021: Forecasting remote atmospheric responses to decadal Kuroshio stability transitions. *J. Climate*, **34**, 379–395, https://doi.org/10.1175/JCLI-D-20-0139.1.

Skamarock, W. C., 2004: Evaluating mesoscale NWP models using kinetic energy spectra. *Mon. Wea. Rev.*, **132**, 3019–3032, https://doi.org/10.1175/MWR2830.1.

——, and Coauthors, 2008: A description of the advanced research WRF version 3. NCAR Tech. Note NCAR/TN-475+STR, 113 pp., https://doi.org/10.5065/D68S4MVH.

Small, R. J., R. A. Tomas, and F. O. Bryan, 2014: Storm track response to ocean fronts in a global high-resolution climate model. *Climate Dyn.*, **43**, 805–828, https://doi.org/10.1007/s00382-013-1980-9.

——, F. O. Bryan, S. P. Bishop, and R. A. Tomas, 2019a: Air–sea turbulent heat fluxes in climate models and observational analyses: What drives their variability. *J. Climate*, **32**, 2397–2421, https://doi.org/10.1175/JCLI-D-18-0576.1.

——, R. Msadek, Y. Kwon, J. F. Booth, and C. Zarzycki, 2019b: Atmosphere surface storm track response to resolved ocean mesoscale in two sets of global climate model experiments. *Climate Dyn.*, **52**, 2067–2089, https://doi.org/10.1007/s00382-018-4237-9.

——, F. O. Bryan, S. P. Bishop, S. Larson, and R. A. Tomas, 2020: What drives upper-ocean temperature variability in coupled climate models and observations. *J. Climate*, **33**, 577–596, https://doi.org/10.1175/JCLI-D-19-0295.1.

Smirnov, D., M. Newman, M. A. Alexander, Y.-O. Kwon, and C. Frankignoul, 2015: Investigating the local atmospheric response to a realistic shift in the Oyashio sea surface temperature front. *J. Climate*, **28**, 1126–1147, https://doi.org/10.1175/JCLI-D-14-00285.1.

Song, H., J. Marshall, D. J. McGillicuddy, and H. Seo, 2020: Impact of current-wind interaction on vertical processes in the Southern Ocean. *J. Geophys. Res. Oceans.*, **125**, e2020JC016046, https://doi.org/10.1029/2020JC016046.

Song, Q., P. Cornillon, and T. Hara, 2006: Surface wind response to oceanic fronts. *J. Geophys. Res.*, **111**, C12006, https://doi.org/10.1029/2006JC003680.

Soufflet, Y., P. Marchesiello, F. Lemarié, J. Jouanno, X. Capet, L. Debreu, and R. Benshila, 2016: On effective resolution in ocean models. *Ocean Modell.*, **98**, 36–50, https://doi.org/10.1016/j.ocemod.2015.12.004.

Swanson, K. L., and R. T. Pierrehumbert, 1997: Lower-tropospheric heat transport in the Pacific storm track. *J. Atmos. Sci.*, **54**, 1533–1543, https://doi.org/10.1175/1520-0469(1997)054<1533:LTHTIT>2.0.CO;2.

Takatama, K., and N. Schneider, 2017: The role of back pressure in the atmospheric response to surface stress induced by the Kuroshio. *J. Atmos. Sci.*, **74**, 597–615, https://doi.org/10.1175/JAS-D-16-0149.1.

Tamsitt, V., L. D. Talley, M. R. Mazloff, and I. Cerovečki, 2016: Zonal variations in the Southern Ocean heat budget. *J. Climate*, **29**, 6563–6579, https://doi.org/10.1175/JCLI-D-15-0630.1.

Tsugawa, M., and H. Hasumi, 2010: Generation and growth mechanism of a Natal pulse. *J. Phys. Oceanogr.*, **40**, 1597–1612, https://doi.org/10.1175/2010JPO4347.1.

Ulbrich, U., and P. Speth, 1991: The global energy cycle of stationary and transient atmospheric waves: Results from ECMWF analyses. *Meteor. Atmos. Phys.*, **45**, 125–138, https://doi.org/10.1007/BF01029650.

Vannière, B., A. C. H. Dacre, and T. Woollings, 2017: A "cold path" for the Gulf Stream–troposphere connection. *J. Climate*, **30**, 1363–1379, https://doi.org/10.1175/JCLI-D-15-0749.1.

Verdy, A., and M. R. Mazloff, 2017: A data assimilating model for estimating Southern Ocean biogeochemistry. *J. Geophys. Res. Oceans*, **122**, 6968–6988, https://doi.org/10.1002/2016JC012650.

Walker, N. D., 1990: Links between South African summer rainfall and temperature variability of the Agulhas and Benguela Current systems. *J. Geophys. Res.*, **95**, 3297–3319, https://doi.org/10.1029/JC095iC03p03297.

Wallace, J. M., T. P. Mitchell, and C. Deser, 1989: The influence of sea surface temperature on surface wind in the eastern equatorial Pacific: Seasonal and interannual variability. *J. Climate*, **2**, 1492–1499, https://doi.org/10.1175/1520-0442(1989)002<1492:TIOSST>2.0.CO;2.

Willison, J., W. A. Robinson, and G. M. Lackmann, 2013: The importance of resolving mesoscale latent heating in the North Atlantic storm track. *J. Atmos. Sci.*, **70**, 2234–2250, https://doi.org/10.1175/JAS-D-12-0226.1.

Yanai, M., S. Esbenson, and J. H. Chu, 1973: Determination of bulk properties of tropical cloud clusters from large-scale heat and moisture budget. *J. Atmos. Sci.*, **30**, 611–627, https://doi.org/10.1175/1520-0469(1973)030<0611:DOBPOT>2.0.CO;2.

Yang, H., P. Chang, B. Qiu, Q. Zhang, Z. C. L. Wu, and H. Wang, 2019: Mesoscale air–sea interaction and its role in eddy energy dissipation in the Kuroshio Extension. *J. Climate*, **32**, 8659–8676, https://doi.org/10.1175/JCLI-D-19-0155.1.

Zhai, X., H. L. Johnson, D. P. Marshall, and C. Wunsch, 2012: On the wind power input to the ocean general circulation. *J. Phys. Oceanogr.*, **42**, 1357–1365, https://doi.org/10.1175/JPO-D-12-09.1.

Zhang, C., Y. Wang, and K. Hamilton, 2017: Projected future changes of tropical cyclone activity over the western North and South Pacific in a 20-km-mesh regional climate model. *J. Climate*, **30**, 5923–5941, https://doi.org/10.1175/JCLI-D-16-0597.1.

——, X. Ma, and L. Wu, 2019: Effect of mesoscale oceanic eddies on extratropical cyclogenesis: A tracking approach. *J. Geophys. Res. Atmos.*, **124**, 6411–6422, https://doi.org/10.1029/2019JD030595.